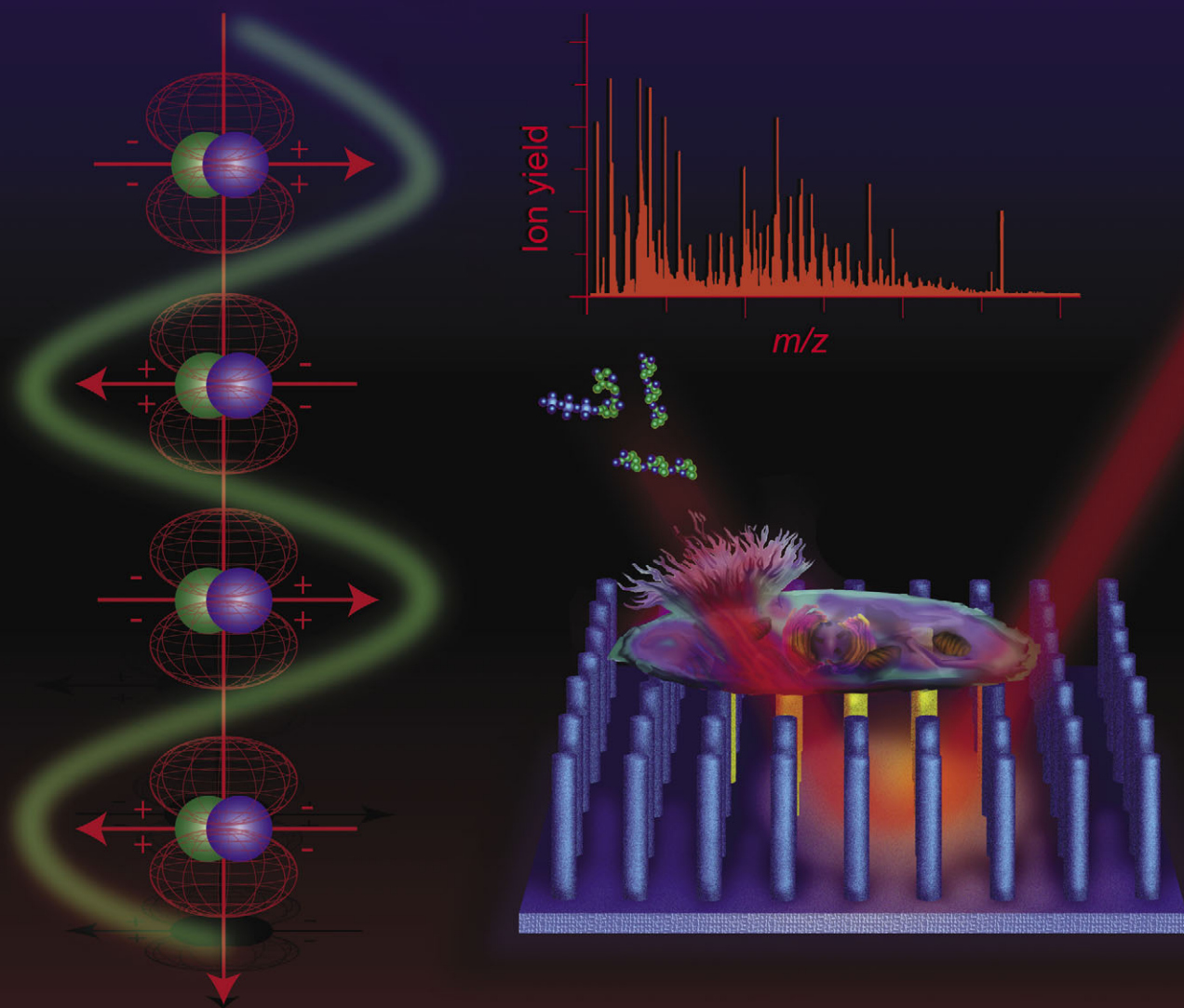


PCCP

Physical Chemistry Chemical Physics

www.rsc.org/pccp

Volume 14 | Number 24 | 28 June 2012 | Pages 8437–8752



ISSN 1463-9076

COVER ARTICLE

Vertes *et al.*
Laser–nanostructure interactions for ion production

HOT ARTICLE

Brown and Hillman
Electrochromic enhancement of latent fingerprints by poly(3,4-ethylenedioxythiophene)



1463-9076(2012)14:24;1-S

Cite this: *Phys. Chem. Chem. Phys.*, 2012, **14**, 8453–8471

www.rsc.org/pccp

Laser–nanostructure interactions for ion production

Jessica A. Stolee,^{†a} Bennett N. Walker,^{†a} Vassilia Zorba,^b Richard E. Russo^b and Akos Vertes^{*a}

Received 5th January 2012, Accepted 17th February 2012

DOI: 10.1039/c2cp00038e

Interactions between pulsed laser radiation and nanostructured materials, with dimensions ranging from 1 nm to 500 nm, can result in enhanced desorption and ionization of organic and biomolecular adsorbates. When the critical dimensions of the nanostructures fall below the characteristic lengths for the involved transport processes, novel regimes of ion production are observed. Systems with dimensions commensurate with the wavelength of the laser radiation are the basis of photonic ion sources with unique properties, including polarization dependent ion yields and fragmentation. The main characteristics of these systems are often governed by altered modes of transport, *e.g.*, ballistic *vs.* diffusive, energy confinement, plasmon resonances, and local field enhancements. Some structures offer control over the internal energy and the active fragmentation channels for the produced ions. Emerging applications of photonic ion sources in mass spectrometry benefit from ultrahigh sensitivity, a wide dynamic range for detection and quantitation, and a broad coverage of adsorbates ranging from small organic molecules to biopolymers, as well as to highly complex samples like single cells.

1 Introduction

The production of molecular ions is a prerequisite for surface sputtering, ion implantation, ion mobility measurements, and mass spectrometry (MS), a powerful method for material analysis.

To enable continued advances in molecular biology, a great deal of effort went into developing ion sources capable of generating intact ions from molecules of biological significance. The type, variety, and abundance of ions in these experiments depend on the nature of the ionization process. Although ion production accompanies almost all forms of energy deposition, useful ion sources have to produce molecular, fragment, and atomic ions with high efficiency. Traditional methods include electron impact ionization, chemical ionization, field ionization, fast atom bombardment, and ion sputtering, whereas newer

^a Department of Chemistry, The George Washington University, Washington, DC 20052, USA. E-mail: vertes@gwu.edu; Fax: +1 202-994-5873; Tel: +1 202-994-2717

^b Lawrence Berkeley National Laboratory, Berkeley, CA 94720, USA

† These authors contributed equally to this work.



Jessica A. Stolee

Jessica Stolee obtained her BS degree in Chemistry from the George Washington University in 2003. She continued on at the George Washington University in pursuit of her Ph.D. She is currently a fifth year Ph.D. candidate working under the direction of Professor Akos Vertes. Her work is focused on the development and fundamental understanding of novel ionization techniques, including nanophotonic ion sources, for mass spectrometry.

Research she conducted at GW and Oak Ridge National Laboratory led to the development of nanopost arrays (NAPA) and three patent applications in which she is a co-inventor.



Bennett N. Walker

Bennett Neave Walker obtained his B.S. degree in chemistry from Trinity College, Connecticut in 2006. He then joined the research laboratory of Professor Akos Vertes at the Department of Chemistry of the George Washington University, Washington, DC. He is currently a 6-th year Ph.D. candidate focusing on the development, understanding, and applications of nanophotonic ion sources for mass spectrometry. Recently, he has utilized these powerful laser ionization platforms for the direct analysis of single microbial cells.

techniques comprise soft laser desorption ionization (LDI) and electrospray ionization. An ionization method is considered soft if it results in limited or no fragmentation, *i.e.*, there is a limited increase in the internal energy during ionization.

Conventional techniques, such as electron impact ionization and some of the early soft ionization methods, *e.g.*, fast atom bombardment, exhibited an upper mass limit between 500 and 5000 Da. This was inadequate for the ionization of proteins, nucleic acids and other biopolymers. In the late 1980s, it was discovered that a UV-absorbing matrix could be used to facilitate the desorption and ionization of large biomolecules.^{1,2} Tanaka's Nobel Prize-winning discovery was based on using a mixture of 30 nm cobalt nanoparticles and glycerol as the matrix. The corresponding method, later named matrix-assisted laser desorption ionization (MALDI), became indispensable for the MS of large molecules.³ Due to matrix-related ions however, spectral interferences in the low mass range made the analysis of small molecules difficult.

To benefit from the advantages of soft laser ionization without the production of high intensity matrix ions, a search

for matrix-free soft LDI platforms ensued. Advances in nanotechnology raised the prospect of producing nanoscopic structures that efficiently utilized the laser pulse energy for the production of ions exclusively from the adsorbates. These matrix-free systems are promising candidates that minimize spectral interferences and improve ionization efficiency.

The interaction of laser radiation with nanomaterials and nanostructures gives rise to unique processes that are not observed in bulk materials or at unstructured surfaces. The main sources of these specific processes include altered energy levels and band structure, confinement effects that result in anomalous transport in the nanostructures, as well as nanophotonic interactions between the laser pulse and the structures. Depending on the material properties, structural dimensions, and laser pulse characteristics, these mechanisms can be manifested in diverse forms. In the first part of this article, we describe the relevant characteristic lengths for the various transport processes associated with the laser–nanostructure interaction and compare them with the critical dimensions of selected nanostructures used as ionization platforms. We demonstrate that the resulting confinement effects can facilitate the production of molecular ions. As the critical dimensions of the nanostructures approach the wavelength of the laser light, which for common laser ionization sources is typically between ~ 100 nm and ~ 10 μm , with the overwhelming majority being in the UV range, nanophotonic interactions emerge. These effects can also result in the production of ions that do not form on unstructured surfaces. In the second part of this article, we demonstrate some of the unique features and applications of laser–nanostructure interactions for ion production.



Vassilia Zorba

Vassilia Zorba is a Research Scientist at the Lawrence Berkeley National Laboratory in Berkeley CA. She received her Ph.D. degree in Physics (2008) from the University of Crete, Greece, under the direction of Professor Costas Fotakis. She then joined the Laser Spectroscopy and Applied Materials Group at the Lawrence Berkeley National Laboratory as a Postdoctoral Fellow. Her research interests include nanoscale ultrafast laser near-and far-field spectroscopy and ultrafast laser-based material functionalization.

1.1 Characteristic lengths and critical dimensions

As most laser ionization sources rely on irradiation of ~ 1 ns to ~ 100 ns pulse length, unless otherwise stated, we restrict our discussion to such excitation sources. Whereas this admittedly excludes ultrafast lasers and the related phenomena,



Richard E. Russo

Dr. Russo is founder and scientific director of the laser material interactions group at the Lawrence Berkeley National Laboratory. His group has pioneered the development of laser ablation for chemical analysis, with an almost 30 year contribution to fundamental and applied research topics, with over 200 refereed scientific publications. Fourteen students have received their PhD degree under his direction at the University of California, Berkeley. Dr. Russo

also is president and founder of Applied Spectra, Inc. The company manufactures analytical instruments using LIBS and Laser Ablation with ICP-OES and ICP-MS.



Akos Vertes

Dr. Akos Vertes is Professor of Chemistry, and of Biochemistry and Molecular Biology at the George Washington University in Washington, DC. He is co-founder and co-director of the W. M. Keck Institute for Proteomics Technology and Applications. His research interests span fundamental studies in physical chemistry to development of new technologies for biomedical analysis. His research has been presented in over 130 peer-reviewed publications, two books, and

numerous conferences. His honors and awards include the Velmer A. Fassel Lecture in Analytical Chemistry, Fellow of the Royal Flemish Academy for Science and the Arts in Brussels, and Doctor of the Hungarian Academy of Sciences.

sporadic experiments with femtosecond excitation for MALDI show inferior ion yields compared to nanosecond pulses.⁴

Irradiation of surfaces with submicrometre features by nanosecond UV laser pulses induces highly nonlinear processes. Due to the rapid energy deposition, optical, electronic, vibrational, thermal, mechanical, and chemical changes are induced in the irradiated material. The extent and contribution of these altered characteristics to ion production depend on the substrate, adsorbate, and laser pulse properties. For example, in the most commonly used soft laser ionization method, MALDI, the desorption step starts with a rapid phase transition that releases the biomolecule or the corresponding ion from the matrix^{5–7} followed by in-plume ionization.^{8,9} The relevant material parameters for the phase transition include the optical absorption coefficients of the substrate and the plume, α_s and α_p , respectively, surface reflectivity, R , the temperature and enthalpy of the phase transition, T_{pht} and ΔH_{pht} , respectively, and the thermal diffusivity, κ , whereas the essential laser parameters are the wavelength, λ , pulse length, τ_p , and fluence, F . In addition, the in-plume ionization processes are governed by the state-to-state absorption coefficients and lifetimes, the ionization potentials of the various molecular and cluster species, the ion recombination rates, and the exciton pooling rate coefficients.¹⁰ An early observation of the role of characteristic lengths and critical dimensions is the example of preferential ion production from thin or small matrix crystals.¹¹ In this case for a crystallite thinner or smaller than the thermal dissipation length, A_t , which is typically $\sim 2 \mu\text{m}$ in MALDI, the surface temperature dramatically rises and the crystallite superheats and completely volatilizes resulting in high ion yields. This process illustrates how the confinement of the deposited laser energy in small crystals can result in enhanced ion production.

Similarly, in nanomaterials and nanostructures a wide variety of confinement effects can be observed. Table 1 lists the corresponding characteristic lengths most relevant for laser–nanostructure interactions: electron wavelength and mean free path, optical absorption length, phonon mean free path, thermal dissipation length, exciton diffusion length, near-field range, the dimensions of plasmon excitations, and the plume expansion length. The typical characteristic length

ranges are calculated based on typical material parameters for metals (Au, Ag, and Pt), semiconductors (Si and Ge) and wide bandgap semiconductors (ZnO) used in soft laser ionization experiments. Whenever a particular dimension of a nanostructure falls below a characteristic length, confinement of electrons, phonons, excitons, plasmons, the laser plume, or the electromagnetic field can occur. The presence of a confinement can significantly alter the laser–nanostructure interaction dynamics by producing field enhancements, high heating rates and prolonged interaction times, and promote ionization.

Fig. 1 shows the relationship between the estimated overall ranges of characteristic lengths, and the critical dimensions of some nanostructures used in soft laser ionization. As nanostructures can, and often do have high aspect ratios, the critical dimension is defined as the thinnest, shortest, or smallest feature that limits the size of a quasi-particle or the flux in a transport process. In the case of nanoparticles, nanowires, nanorods, and nanoposts the critical dimension corresponds to their diameter. The near-field range is determined by the aspect ratio of the smallest feature in the structure or the diameter of an aperture. With respect to redistribution of the deposited energy, for nanopores and nanowells the critical dimension is the thickness of the material between the pores or wells. In terms of plume dynamics, however, the pore diameter can be viewed as the critical dimension.

Nanoparticles of metals and semiconductors comparable in size to the electron wavelength exhibit altered energy levels, which has a direct effect on their optical properties. Due to the changes in their absorption spectrum these quantum dot particles show size dependent colors. In principle, adjusting the particle size and/or shape to exhibit enhanced absorption at the laser wavelength can facilitate the energy deposition (see Fig. 3a and b).¹²

For nanoparticles with diameters less than 5 nm, the electron wavelength significantly influences the spatial distribution of the deposited energy.¹³ For larger structures, with critical dimensions up to 100 nm, other characteristics, such as the electron mean free path, which ranges from 1 nm to 100 nm, the optical penetration depth, and the exciton diffusion length can alter the laser–nanostructure interactions. For particles that are smaller than the electron mean free path, surface plasmons

Table 1 Typical ranges for characteristic lengths depicted in Fig. 1 are calculated using the equations shown here. The values are derived for metals (based on data for Ag, Au and Pt), semiconductors (represented by Si and Ge) and wide bandgap semiconductors (using data for ZnO), the absorption coefficient, α , values are obtained for $\lambda = 337 \text{ nm}$ and the thermal dissipation lengths are calculated assuming $\tau = 4 \text{ ns}$. In these equations $k_F =$ Fermi wave vector, $v_F =$ Fermi velocity, $t_s =$ scattering time, $\lambda =$ wavelength, $D_e =$ exciton diffusion constant, $\tau_{\text{exc}} =$ recombination lifetime, $\kappa =$ thermal conductivity, $C_v =$ volumetric heat capacity, $c_s =$ speed of sound in the material, $\tau =$ laser pulse length, $\rho =$ density of material, $C_p =$ specific heat capacity of the material, and $A_{\text{nf}} =$ near field range

Characteristic length	Equation	Confinement	Typical ranges/nm		
			Metals	Semiconductors	Wide bandgap semiconductors
Electron wavelength	$\lambda_e = \frac{2\pi}{k_F}$	Electron	<1	1–5	1–5
Electron mean free path	$l_e = v_F t_s$	Energy	1–30	10–100	10–100
Exciton diffusion length	$A_e = \sqrt{D_e \tau_{\text{exc}}}$	Energy	n/a^a	10–100	0.1–25
Phonon mean free path	$l_p = \frac{3\kappa}{C_v c_s}$	Energy	5–200	200–300	10
Thermal dissipation length	$A_t = 2\sqrt{\frac{\kappa}{\rho C_p}}$	Energy	50–200	50–150	40
Optical absorption length	$A = \frac{l}{\alpha}$	Electro-magnetic radiation	10–30	> 10	> 60
Near-field range	$A_{\text{nf}} \leq \lambda$	Electro-magnetic radiation	100–10 000	100–10 000	100–10 000

^a In some metals (Ag, Cu and Au) transient excitons do exist for short periods after ultrafast laser excitation.^{194,195} Time-resolved two-photon photoemission shows that in Au their lifetimes are in the < 300 fs range.¹⁹⁶

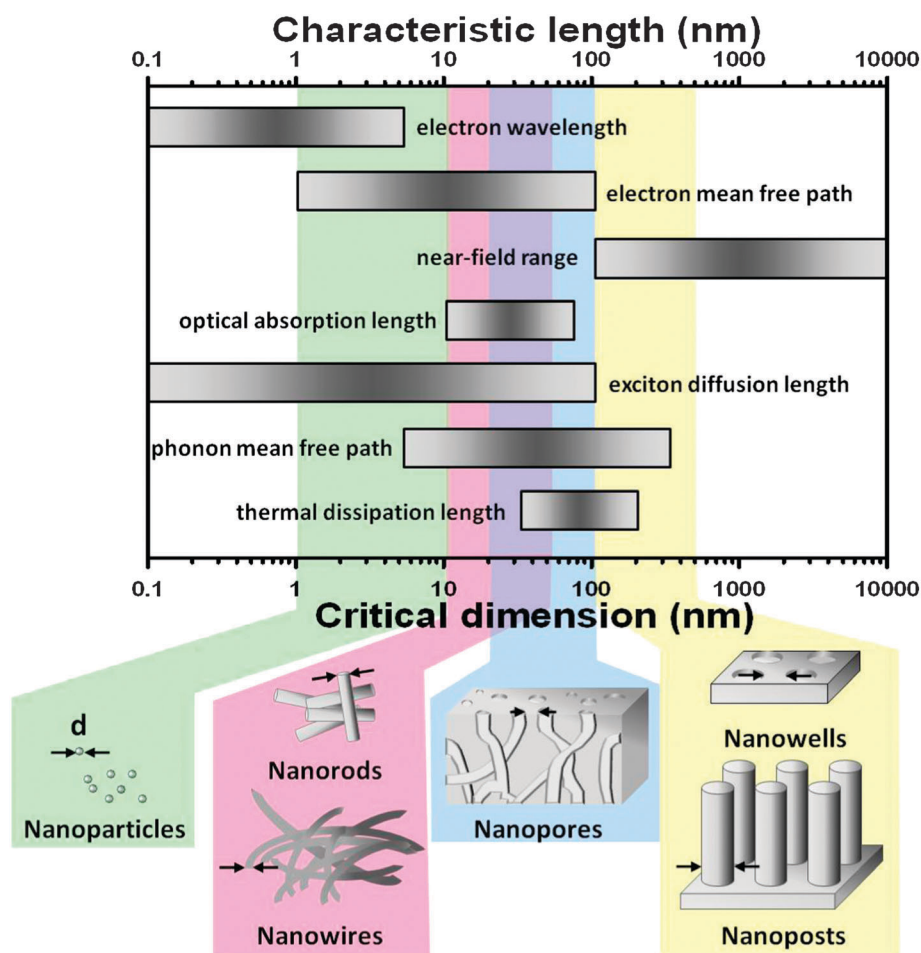


Fig. 1 Characteristic length ranges for energy and charge carriers that are relevant in the transport properties of nanostructures. Some nanostructures used in laser desorption ionization are depicted and their critical dimensions are indicated with arrows.

can be created with dimensions that depend on the shape, size, and dielectric constant of the material.¹⁴

The depth that electromagnetic radiation can penetrate a conducting surface is described as the skin depth. This parameter is dependent on the frequency of the radiation and the resistivity of the material. For conducting surfaces irradiated with light of 337 nm wavelength, the skin depth typically ranges from 2 nm to 100 nm. Structures that have critical dimensions similar to or smaller than the skin depth will undergo rapid heating and exhibit a uniform temperature. For structures larger than the skin depth, a transient temperature gradient in the structure is observed.¹⁵

The distance that excitons can travel to donor or acceptor interfaces is typically between 0.1 nm and 100 nm.¹⁶ This exciton diffusion length is a particularly important characteristic for organic semiconductors and is thought to affect the ionization mechanism in MALDI.¹⁷ Excitons within nanostructures may also influence the interaction between the surface and adsorbate during the ionization process.

For nanostructures with critical dimensions from 5 nm to 500 nm, the optical absorption length, phonon mean free path, and the thermal dissipation length influence energy absorption and dissipation. Heat transport in objects larger than the phonon mean free path (5 nm to 300 nm depending on the material) is diffusive, whereas objects with critical dimensions that are

comparable to or smaller than the mean free path exhibit partially or completely ballistic transport.¹⁸ The distance heat is transported within bulk material during the laser pulse is described by the thermal dissipation length and is dependent on the thermal conductivity, heat capacity, and density of the material as well as the laser pulse duration. The thermal dissipation length for Q-switched laser pulses, with typical pulse lengths in the low nanosecond range, falls between 40 nm and 200 nm.¹⁹

Fig. 1 indicates how the characteristic lengths that govern the deposition, redistribution and dissipation of energy in nanostructures relate to their critical dimensions. As the critical dimensions of the nanostructures diminish, they fall below more and more characteristic lengths. This gives rise to the onset of multiple confinement phenomena and increasingly exotic interactions with the laser radiation. For example, it is thought that ion generation from a silicon nanopost array (NAPA) is simultaneously controlled by the near field enhancement of the electromagnetic field, radial confinement of the deposited energy in the posts, and plume confinement of the desorbed material in the troughs between the posts.²⁰

1.2 Nanostructures as ion sources

A variety of nanomaterials and nanostructures have been proposed as matrix-free LDI platforms. One of the first broadly adopted approaches was desorption ionization on

Table 2 Abbreviations used for nanostructure-based and some other common ionization sources in MS

Acronym	Resolved form	References
DESI	Desorption electrospray ionization	197, 198
DIOS	Desorption ionization on silicon	21, 23, 139
DIOSTA	Desorption and ionization from silicon tip arrays	46
ESI	Electrospray ionization	199–201
GALDI	Graphite-assisted laser desorption ionization	37, 41
LAESI	Laser ablation electrospray ionization	202–204
LISMA	Laser-induced silicon microcolumn array	24, 42, 133
MALDI	Matrix-assisted laser desorption ionization	2, 205, 206
NALDITM	Nanowire-assisted laser desorption ionization	28, 132
NAPA	Nanopost array	20, 43, 44
NIMS	Nanostructure initiator mass spectrometry	147, 165
SALDI	Surface-assisted laser desorption ionization	39, 127, 129
SiNW	Silicon nanowire	28, 132

porous silicon (DIOS) (see Table 2 for abbreviations for common ionization sources).^{21–23} Now, other disordered monolithic silicon ionization sources include microcolumns,²⁴ nanodots,²⁵ nanowires,^{26–30} nanoparticles,³¹ nanofilms,³² and a few other types of nanostructures.³³ In addition to silicon, nanostructures from materials such as Au,^{29,32} Ag,³⁴ Ge,^{35,36} C,³⁷ and Pt³⁸ have also entered the field. Surface-assisted laser desorption ionization (SALDI)^{39,40} and graphite-assisted laser desorption ionization (GALDI)^{37,41} were primarily developed for particular applications. Apart from minimizing matrix interferences, nanostructures are found to significantly improve sensitivity, *e.g.*, exhibiting detection limits as low as 800 ymol (yoctomoles),²³ enhance selectivity, and enable adjustable fragmentation.^{42,43}

Ordered monolithic structures, such as NAPA,⁴⁴ nanocavity arrays,⁴⁵ and nanoposts⁴⁶ can also be produced using nanofabrication protocols. Exquisite control over their dimensions makes these structures ideal for studying the mechanisms involved in the desorption and ionization processes. It also enables the optimization of the ion yields as a function of the established critical dimensions.

In this perspectives article we discuss how the characteristic dimensions and relevant material properties affect laser–nanostructure interactions and the subsequent desorption and ionization processes. A separate section is devoted to some of the emerging applications.

2 Desorption and ionization processes on the nanoscale

The discussion of laser–nanostructure interactions can follow the same three phases used to describe ion production from non-structured surfaces. The driving force behind these processes is the energy deposition from the laser pulse into the nanostructure. From the fundamental principles governing laser energy deposition, we turn our attention to the energy redistribution within nanostructures and between the substrate and the adsorbates. The third subsection deals with desorption and the formation of molecular and fragment ions. Although we discuss these steps in sequence, in reality some of these processes take place simultaneously.

2.1 Laser energy deposition—optical properties

When laser radiation impinges on a solid target, the initial phase of the interaction can be viewed as energy deposition. According to the conservation of energy, the reflectance R ,

absorbance, A , and transmittance, T , satisfy $R + A + T = 1$. In many of the LDI experiments $T \approx 0$, *i.e.*, no significant transmission occurs, thus we focus our attention on the reflection and absorption processes.

Whereas the intrinsic values of reflectance and absorbance at low light intensities are defined by the properties of the bulk material in the linear regime, the elevated laser intensities present in these experiments frequently invoke a non-linear response, for example, the saturation of absorption, shifting of the absorption maximum, the generation of harmonics, and luminescence up-conversion. Further complications arise because the optical properties of the target can be modified by the laser radiation. These often transient changes are induced by the heating of the target, the photogeneration of charge carriers, and the shifting of energy levels.

Nanomaterials and nanostructures can exhibit altered optical properties both in the linear and nonlinear regime. Some of these changes stem from the increased surface-to-volume ratio, whereas others are the result of the splitting and increased spacing of energy levels, or the transformation of the density of states in reduced dimension materials. For nanostructures with reduced critical sizes and increased aspect ratios, these effects intensify.

These changes have far reaching consequences not only for the optical but for thermal and other material properties. A detailed discussion on this topic for semiconductors and other nanomaterials is described in an excellent recent monograph.⁴⁷ In this section we restrict the discussion to the optical behavior most relevant for laser–nanostructure interactions.

Reflection. The wavelength corresponding to the main inter-band transition scales with the bandgap. Therefore, in the wide range between the band edge and the optical phonon energies, insulators with no particular resonances are transparent. At light intensities in the linear regime, insulators show low reflectivity, whereas semiconductors and especially metals below the plasma frequency are highly reflective.

Due to the more frequent electron–phonon collisions at elevated temperatures, heating a metal target by a laser results in significantly reduced reflectivity.⁴⁸ The reflectivity of copper and aluminium close to their melting points drops from 0.95 and 0.82, respectively, at room temperature to 0.75 and 0.65, respectively.⁴⁹ In semiconductors, the most important change in the optical response is due to the generation of free carriers. For example, in silicon the electron–hole plasma produced by the laser pulse dissipates its energy through interactions

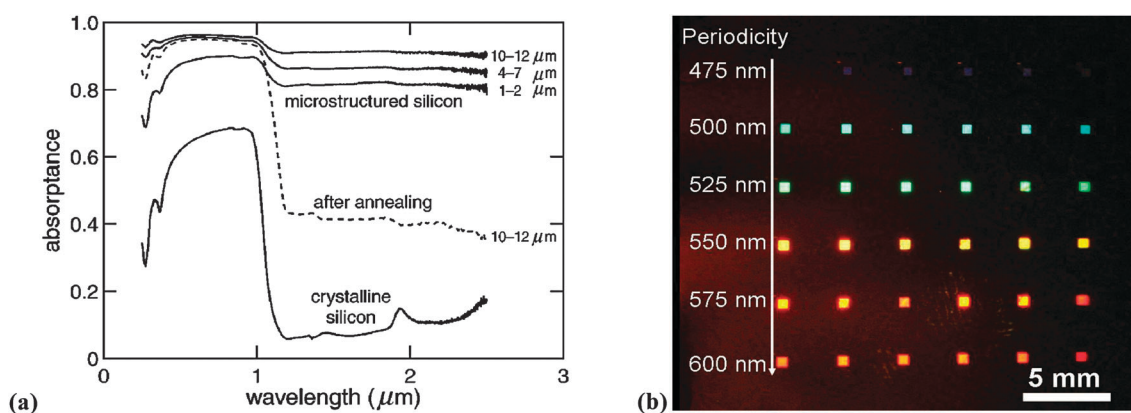


Fig. 2 (a) Absorbance of microstructured silicon with various feature sizes remains close to unity even below the band gap ($\lambda > 1.1 \mu\text{m}$). A comparison is made with crystalline silicon and with microstructured silicon after annealing, where the absorbance drops significantly for wavelengths below the band gap. Reprinted with permission from ref. 193. Copyright [2001], American Institute of Physics. (b) White light illumination of a silicon wafer with thirty-six NAPAs show strong specular reflection of different colors as the periodicities vary between $P = 475$ and 600 nm .

with the phonons, which, above a threshold fluence, results in transient melting.⁵⁰

When the optical absorption length in the material becomes commensurate with the critical dimension of the nanostructure, the energy stored in surface plasmon excitations can become significant. This, in turn, results in a dramatic drop in the reflectivity at a certain angle or wavelength corresponding to resonance conditions. This resonance is extremely sensitive to the magnitude of the critical dimension, *e.g.*, the layer thickness for thin films, and even to the presence of adsorbates. In the case of silver nanoparticle films, reducing the particle size from 50 nm to 35 nm and below also resulted in significantly reduced reflectance between the band edge and 800 nm .⁵¹ Silicon nanotips, with base diameters of $\sim 200 \text{ nm}$, exhibit low reflectivity all the way into the terahertz region.⁵²

Nanophotonic structures, with periodicity commensurate with the wavelength of excitation, exhibit strong specular reflectance (see Fig. 2b), whereas in other directions the reflectivity is reduced. Light scattering is often measured as part of the diffuse reflectance. As the size of nanoparticles or structures approach the wavelength of the light, Mie scattering can become significant. Further reducing the dimensions of scatterers results in Rayleigh scattering. Because the density of scatterers in these systems is large, a multiple scattering approach is necessary to account for the observations. For quasi-one-dimensional systems, *e.g.*, nanowires and nanorods, with lengths comparable to or larger than the wavelength of the light, scattering can become strong enough to complicate absorption measurements. Due to the presence of surface plasmons, scattering from silver nanoparticle dimers, trimers, or tetramers can lead to staggering intensity enhancement, directionality, and polarization of the scattered light.^{53,54}

Absorption. Light absorption in bulk materials is associated with the excitations of atomic, molecular and quasiparticle, or collective energy levels. The absorption length is dependent on the laser wavelength and the material parameters, *i.e.*, the conductivity and dielectric function. Energy deposition by an ultraviolet laser penetrates metal and semiconductor targets to depths of 1 to 60 nm at room temperature. During absorption,

the conduction-band and valence-band electrons are excited by the photons, producing plasmon excitations. Other quasiparticles, such as polaritons and polarons, may also be excited.

As we have mentioned, in the absence of specific resonances, insulators and semiconductors between the band edge and the optical phonon energies are transparent. Laser excitation, however, can create electron-hole pairs and excitons that dissipate their energy by radiative and nonradiative recombination. Relaxation of the electrons, *via* collisions in the lattice, occurs on a sub-picosecond timescale. The electronic structure, defect states, and the bandgap energy of semiconductors and insulators will determine the response of the lattice to excitation. Delocalized processes, *i.e.*, electron-phonon scattering, are the primary means of relaxation in homopolar semiconductors and metals, and electron-electron scattering and localized processes are less probable.

The reduction in size to meso- and nanostructured materials has a pronounced effect on the electronic states resulting in increased energy level spacing in the band diagram. In reduced dimension systems, *e.g.*, quantum wells, wires, and dots, the density of electronic states goes from a continuum to discrete values.⁴⁷ This also leads to the departure of the optical properties from the bulk values. For example, meso-structured silicon surfaces, such as laser-induced silicon microcolumn arrays (LISMA), exhibit close to unity absorbance from the near-ultraviolet to the near-infrared⁵⁵ and the luminescence from such structures is attributed to recombination emissions from the defect centers and quantum confinement.⁵⁶ A comparison of the absorbance of microstructured silicon and crystalline silicon is shown in Fig. 2a. At wavelengths below the band gap energy ($\lambda > 1.1 \mu\text{m}$) the absorbance of crystalline silicon drastically drops, whereas the absorbance of the microstructured silicon remains close to unity.

When the size of the structure is smaller than the exciton diffusion length and commensurate with the electron wavelength, which is typically an order of magnitude smaller for metals than semiconductors, quantum size effects arise. Quantum confinement is observed in porous silicon (with a crystallite size of a few nanometres),⁵⁷⁻⁶⁰ semiconductor quantum dots,⁶¹ small metallic particles,⁶² and quantum wires.⁶³ The dimensions of these

nanostructures can be changed to tune the bandgap and the optical properties, such as photoluminescence, of the material.^{64,65}

In nanowires with critical dimensions less than 100 nm, the absorption and emission of the electromagnetic radiation are strongly polarization dependent. In these structures, the photoluminescence intensity reaches a maximum when light is linearly polarized. This effect is correlated to the large difference in the dielectric constant between the nanostructures and the surrounding environment.^{66–68}

In LDI experiments, the absorption coefficients of the substrate, the adsorbate and, in some cases, the materials in the desorption plume need to be considered. In the ultraviolet region, molecules containing polycyclic aromatic hydrocarbons, primary nucleobases, and aromatic amino acid residues absorb a portion of the radiation *via* $n \rightarrow \sigma^*$ or $\pi \rightarrow \pi^*$ transitions.⁶⁹ For radiation in the mid-infrared range, the OH stretching modes of water exhibit strong absorption. Although absorption by the plume can be important at high laser irradiances, most desorption ionization experiments from nanostructures utilize fluences close to the ionization threshold in the near ultraviolet range (> 300 nm), where biopolymers and many metabolite molecules do not strongly absorb. In this case, the optical properties of the nanostructured material will govern the light absorption mechanism.

2.2 Energy redistribution—thermal properties

Upon laser irradiation of a material at low to moderate fluences, some of the absorbed energy is dissipated through thermal processes, rapidly increasing the temperature of the target. In metals, the excitation of electrons produces a high temperature electron gas which heats the lattice through inelastic electron–phonon scattering.⁷⁰ In semiconductors, electron–hole pairs, generated during photon absorption, thermalize *via* energy exchange with phonons. The optical and thermal properties, such as the absorption and reflection coefficients, and the thermal conductivity of the material govern the heat conduction and resulting surface temperatures. For macroscopic objects, the Fourier heat conduction law can be used to predict the diffusive heat transport of the scattered carriers. Based on the Fourier law, the thermal dissipation length for the duration of a laser pulse can be calculated using the thermal conductivity and heat capacity of the material. As shown in Table 1, for some of the commonly used materials this value ranges between 40 nm and 200 nm for a 4 ns laser pulse. Thus, for substrates with features larger than the dissipation length, a temperature gradient in the target is established.

However, on short time and spatial scales, *i.e.*, when the times are similar to that of the phonon relaxation times and the sizes of the structures are on the scale of the phonon mean free path, which can be as large as 300 nm, heat transport is ballistic in nature.¹⁸ This means that the phonons travel through the structure unimpeded and the scattering events primarily take place at the interface. Therefore, the transport mechanism, and ultimately the thermal properties of the nanostructures used for ion production, are dependent on phonon confinement and boundary scattering.

Thermal conductivity is not only influenced by the size of the system, but also by the temperature.^{71,72} At temperatures above 300 K, phonon–phonon scattering processes dominate

and the thermal conductivity is dependent on the phonon mean free path. In the case of nanostructures, the thermal conductivity is also dependent on the effect of roughness on the phonon–boundary scattering and the size and shape of the structure.^{73–75} For structures with features smaller than the phonon mean free path, exhibiting ballistic transport, *e.g.*, thin silicon nanowires, a significant decrease in the thermal lattice conductivity from the bulk is observed.^{76–78} This is attributed to the enhanced boundary scattering as the dimensions of the structure become smaller.⁷³ For dimensions less than 10 nm, *e.g.*, quantum dots, spatial confinement leads to an increase in phonon relaxation times and the thermal conductivity significantly deviates from the bulk value.⁷⁹ Even for structures with critical dimensions larger than the phonon mean free path, such as nanoposts and nanowells, thermal transport can still be affected. For example, in 3 μm thick single crystal films, the thermal conductivity is still half of the bulk value and can be further decreased by grain boundary scattering.⁸⁰

Electronic thermal conductivity also contributes to the heat conductivity in metals and semiconductors. Due to local and phonon boundary scattering in micro- and nanostructures at or below the electron mean free path, *i.e.*, a few hundred nanometres, a decrease from the bulk electrical conductivity is observed.^{81,82} As the dimensions of the structure become smaller, the thermal conductivity also decreases due to diminishing contributions from the electrons.^{83,84} Additionally, intrinsic surface phenomena, *e.g.*, surface plasmon excitation, can cause deviations from the bulk.

Due to the difficulty in measuring the heating of nanostructures, most surface temperatures are assessed using model calculations. The energy dissipation and surface temperatures of NAPA with different post diameters have been solved for using the Fourier law by including the temperature-dependent thermal conductivity, reflectivity, and specific heat.⁴⁴ Calculations for posts ranging from 50 to 800 nm in diameter confirm that, due to radial energy confinement effects, thinner posts reach higher surface temperatures than larger posts. Measuring ion yields from nanostructures can be used to evaluate the laser induced thermal load on them.⁸⁵

Laser induced phase transitions occur when the material is irradiated to temperatures above its melting threshold. The formation of a transient melt layer alters the reflectivity and surface morphology of the material.^{86,87} Due to evaporation, atoms and particles from the surface of the nanostructure can be removed, which alters the size of the nanostructure. Surface restructuring of porous silicon induced by the laser is thought to play a role in adsorbate desorption and material ablation.⁸⁸ Melting and ablation of nanostructures with critical dimensions smaller than 100 nm can also impact the desorption and ionization mechanism. For example, gold nanoclusters are ablated and detected along with the analyte molecules in some MS experiments.⁸⁹

Near-field effects take place when a macroscopic illumination source interacts with nanostructured surfaces, or when a nanoscale illumination source interacts with a surface. In the latter case, near-field effects become predominant when the nanoscale irradiation source interacts with a surface in its close proximity (optical near-field). This nano-source can be a pulsed laser coupled to a probe tip (apertureless configuration)

or a tapered optical fiber (apertured configuration). In the laser ablation regime, light confinement in the optical near-field leads to non-diffraction limited material modification and represents one of the main strategies for enabling high-spatial resolution laser-ablation based chemical analysis.

Near-field laser ablation-based chemical analysis has been demonstrated in both apertureless and apertured configurations. Elemental analysis with sub-micrometre lateral resolution has been reported for apertureless near-field laser ablation inductively coupled plasma MS.^{90,91} In the apertured near-field scheme, mass spectrometric analysis of molecular solids was performed *via* atmospheric sampling of the ablated material through a capillary interface. A spatial resolution of hundreds of nanometres⁹² to a few micrometres⁹³ was achieved depending on the mass spectrometer configuration used.

In addition to MS-based techniques, laser-induced breakdown spectroscopy (LIBS) has been used for chemical analysis in the near-field. Micrometre-scale spatial resolution has been demonstrated in apertured near-field LIBS,^{94,95} a resolution inferior to that observed in far-field LIBS.⁹⁶ Craters smaller than 30 nm have been reported in apertured near-field laser ablation,⁹⁷ however, the detection of spectral emission in this case is extremely challenging due to the infinitesimal amount of corresponding ablated mass. Interestingly, the structures formed in materials like Si by atmospheric pressure near-field ablation can be tuned between craters and protrusions depending on the laser wavelength or number of pulses,⁹⁷ underlining the importance of laser, material and sampling environment combinations as means to promote/impede certain types of processes (*e.g.*, oxidation).

2.3 Desorption, ionization and fragmentation of adsorbates

Some of the main factors and mechanisms governing desorption, ionization, and fragmentation of adsorbates and surface layers from nanostructures will be described in this section. First we demonstrate some basic principles on laser induced processes at macroscopic surfaces. This is followed by delineating the effects specific to nanoscopic systems and nanophotonic ion production.

The energy deposited by the laser pulse can drive the excitation of electrons, atoms, molecules, and quasiparticles. Depending where a substantial portion of this energy ends up, different desorption ionization mechanisms can be activated. These processes can be driven by exciting the electron gas in a metal substrate, electron-hole pair generation in semiconductors, phonon excitations, generation of excitons (*e.g.*, in MALDI), plasmon excitations, and the electronic excitation of the adsorbate (*e.g.*, in desorption induced by electronic transition (DIET)). Often, the combination of these mechanisms is observed.

Laser desorption ionization from macroscopic surfaces. To understand the essential processes underlying LDI, idealized model systems, based on single crystals exhibiting a well-defined crystallographic plane as the substrate and monolayers of small molecules as adsorbates, were introduced in the 1980s. This enabled well controlled experiments on the angular distribution of final-state resolved ion yields produced by the laser radiation, and the exploration of kinetic and internal energy transfer. Working with simple solids and adsorbates

also allowed the construction of potential energy surfaces and theoretical models to complement the experiments.

Molecules adsorbed on a solid surface experience shifting of their energy levels (physisorption) or the formation of chemical bonds (chemisorption). In turn, some adsorbates restructure the surface.⁹⁸ The stronger the adsorbate-surface interaction the more substantial surface restructuring is observed. Restructuring upon adsorption ranges from relaxation of the reduced bond lengths at the surface closer to the bulk values, to the chemical transformation of the surface layer.

Laser energy deposition into the substrate in the presence of the adsorbate initiates the desorption process through several potential pathways. Laser pulses in the UV and visible range can couple their energy to the electrons in the substrate. The hot electron gas equilibrates with the lattice phonons in a few picoseconds. The phonon excitation mediated processes rely on vibrational energy transfer to release the adsorbate. Laser-induced thermal desorption of H₂ observed from Si(111) and Si(100) surfaces was explained in terms of hydrogen atom migration and recombination on the substrate followed by the departure of the H₂ molecule.⁹⁹

An alternative pathway for desorption is the direct energy transfer from the excited electron gas to the adsorbate. Early observations of internal and kinetic energy distributions in NO desorption from a Pt(111) surface showed that the hot conduction band electrons were responsible for driving the process.^{100,101} Analysis of the results based on semiclassical scattering theory indicated the transient presence of a negative adsorbate ion, NO⁻, that facilitated the desorption process.¹⁰² Ultrafast excitation of the Cu(111) surface covered with CO adsorbates results in hot electron mediated desorption events in less than 325 fs.¹⁰³ In some cases, energy transfer through phonons and electrons results in the desorption of different chemical species. Thermal excitation of the ruthenium substrate with carbon monoxide and oxygen atoms adsorbed on its (0001) surface results in CO desorption, whereas laser excitation of the electrons in the Ru target releases CO₂.¹⁰⁴

If the laser radiation induces an electronic excitation in the adsorbate leading to a repulsive state, a desorption event can result.^{105,106} Investigation of this DIET process gave insight into the role of surface bond orientation and numerous dynamical processes. Desorption of the adsorbate is triggered if it acquires sufficient kinetic energy before returning to the ground state. In order for this to occur, the photon energy needs to exceed the surface bond energy. Since the lifetime of excited states is typically less than a picosecond, the desorption efficiency is low.¹⁰⁷ However, further exciting molecules that are already in the excited state increase the desorption efficiency.

In some insulators, efficient energy deposition into phonons and exciton generation proceed simultaneously. In MALDI, energizing the phonons drives a phase transition in the matrix,^{108,109} while the generated excitons advance the ionization process.^{8,10}

Laser desorption ionization from nanostructures. Nanoscopic protrusions on silicon surfaces are known to result in a significant local enhancement of the electromagnetic radiation. For a 10 : 1 aspect ratio column, this can result in an intensity gain close to 200 in the near-field.¹¹⁰ Metal nanostructures can

exhibit additional enhancements through surface plasmon resonances and operate as optical antennas.^{111–113} These structures demonstrate resonant energy absorption¹¹⁴ that is sensitive to polarization¹¹⁵ and antenna length,¹¹² and their near-field response can be tuned through altering their geometry.¹¹⁶

The absorption of light by noble metal nanoparticles with dimensions smaller than the electron mean free path creates surface plasmons, *i.e.*, a collective oscillation of electrons in the conduction band of the material. This produces enhanced electromagnetic fields and charge interactions that are localized on the surface of the material. The plasmon resonance frequency and intensity is dependent on the size and shape of the metallic nanoparticle.¹⁴ Experiments show that when the desorption laser is near the resonant frequency of the metallic nanoparticles, strong near fields, due to surface plasmons, are induced and facilitate desorption and ionization (see Fig. 3).^{12,117–121}

In recent years, the idea to utilize localized plasmon resonance for LDI has attracted growing attention. Plasmons in gold nanorods^{117,118} and other nanoparticles^{119,120,122–124} have been exploited to shift the energy deposition resonance into the UV, visible, and NIR range.^{12,121} Because the wavelength of energy coupling through localized surface plasmon resonance can be selected by changing the geometry of the nanoparticles, *e.g.*, the aspect ratio of nanorods, an extended selection of lasers can be used for LDI-MS to offer high sensitivity and specificity in biosensor applications.^{125,126}

The desorption step from NAPA structures was probed using preformed ions, *i.e.*, ions that already exist as an adsorbate. As the laser fluence was increased, the fraction of ions that remained intact decreased, indicating enhanced energy transfer.⁴³ Results also demonstrated that the desorption threshold decreased for thinner posts, pointing to the contribution

of a thermal mechanism.²⁰ Other experiments also suggested that rapid heating of the nanostructure was a key factor in the desorption process. For example, for DIOS structures it was found that a minimum surface temperature of 800 K was required to desorb preformed ions from the porous silicon substrates.¹²⁷ It was suggested that desorption was induced by heating the surface rather than direct photoionization by laser irradiation.

Experiments using preformed ions desorbed from ordered nanocavity arrays found that the laser threshold for ion detection depended on the substrate morphology, due to differences in the thermal confinement.⁴⁵ For silicon nanowire (SiNW) substrates, the desorption efficiency of preformed ions at low laser fluences was attributed to the attained high surface temperatures, due to thermal confinement effects.²⁸ In this regime the substrate thermal properties and surface chemistry (*i.e.*, the intentional or inadvertent chemical modification of the nanostructure surface layer) play an important role. For example, no molecular ions were detected from oxidized SiNWs.¹²⁸ The adsorbate ion yields in LDI experiments from various metallic nanoparticles were found to depend on the thermal conductivity of the metal. Using nanoparticles with lower heat conductivity and higher melting temperature promoted ion production.¹⁹ Studies on two-layered nano- and micro-structured surfaces also show that the substrates with lower thermal conductivity and coatings with high absorptivity at the wavelength of the UV laser result in the greatest ion yields.³³ These experiments demonstrate the large influence that the thermal properties of the substrate have on the desorption efficiency.

Desorption of the substrate material and adsorbate can occur *via* a defect-mediated process. Defects alter the electronic structure

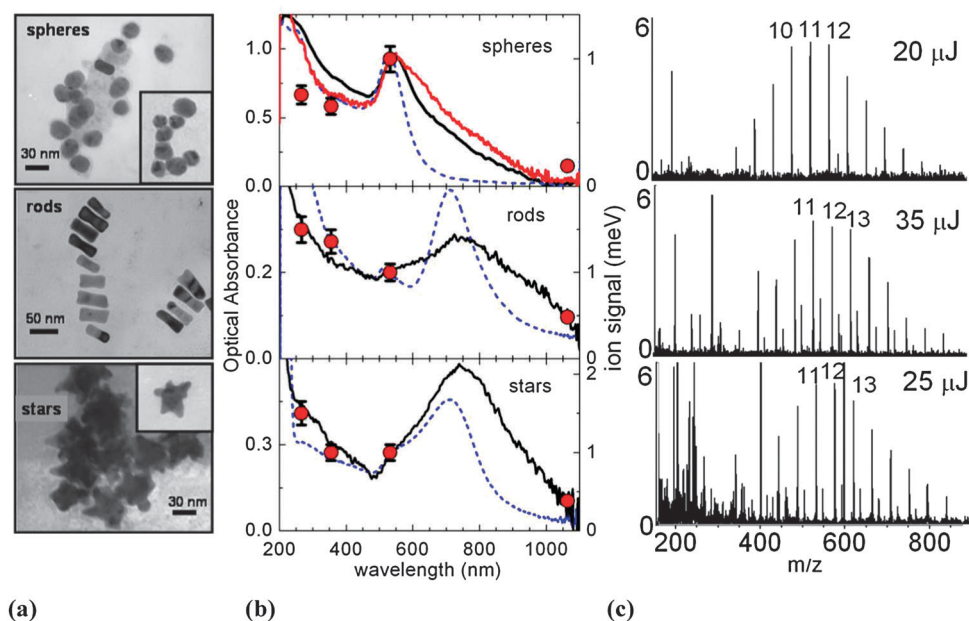


Fig. 3 (a) Transmission electron microscope images of three gold nanoparticle types: (top) spheres, (middle) rods, and (bottom) stars with approximate dimensions of 20 nm, 25 nm (width), and 35 nm (core diameter), respectively. (b) Optical absorbance spectra corresponding to the nanoparticles in aqueous solution (blue dotted lines), in a thin film on quartz (black line), and from a film on nanoparticles precipitated with PEG (red line). Red circles represent the relative inverse fluence thresholds (y -axis on the right). (c) Laser desorption ionization mass spectra at a laser wavelength of 355 nm for PEG600 deposited on the gold nanoparticles. The laser pulse energies are noted in the top right corners. Reprinted with permission from ref. 12. Copyright [2010], Springer.

of the material and affect its optical and vibrational properties. They can also drive desorption by acting as recombination centers for electron–hole pairs or by weakening the bond structure of the lattice. Hole trapping at localized surface vacancies was found to play a role in the desorption of adsorbates from silicon surfaces by changing the surface charge density.¹²⁹

Electromagnetic fields in the vicinity of nanostructures deviate from the far-field values due to the local interactions between the radiation and the structures with features on the order of the wavelength of light or smaller. The resulting highly confined electromagnetic fields can cause the desorption and ionization of molecules.⁹² Analogous to the behavior of macroscopic antennas, the field enhancement depends on the polarization of the incoming radiation and on the length and aspect ratio of the structure.¹³⁰ In the vicinity of high aspect ratio silicon tips, the light intensities were enhanced by more than two orders of magnitude compared to the incident radiation.^{110,131} It was suggested that these strong near-fields induce a desorption process that contributed to the low fluence thresholds for the detection of preformed ions observed from SiNWs.¹³² Evidence from NAPA-MS experiments showed that enhanced near fields around high aspect ratio posts did result in decreased fluence thresholds for LDI.⁴³ Confirmation of truly photonic ion production was found for LISMA and NAPA structures. Ion yields from these substrates were strongly dependent on the plane of polarization of the electromagnetic radiation, also suggesting a behavior similar to energy coupling in optical antennas. In the case of p-polarized laser pulses, ion yields exhibited a maximum, whereas s-polarized radiation resulted in vanishing ion production.^{20,133}

Another mechanism, termed field ionization, has been proposed for laser desorption and ionization platforms with nanoscopic protrusions.^{35,132,134} Here, the applied electric field causes charge accumulation in the protruding structures, where, depending on the interaction strength between the surface and adsorbate, molecules can be desorbed.¹³⁵ Since the surface charge density decreases with increasing size, it is critical that the protruding structures have fine tips or sharp edges to produce the very high fields required for field desorption. The applied electric field also increases the energy of the electrons in the atoms near the surface, causing electron tunneling and resulting in adsorbate ionization.

Depending on the characteristic dimensions and surface roughness of the nanostructure, the particles in the desorbed plume may experience confinement within its cavities and crevices. If the diameter of nanoscale pores is close to the size of the molecules, then the surface–adsorbate interactions may be altered resulting in phase transitions and long range density fluctuations.^{136,137} Computational modeling reveals that higher primary ion yields are observed from porous substrates than from less structured surfaces.¹³⁸ In nanostructures with high aspect ratios, entrapment of the sample within the structure may occur.¹³⁹ In this scenario, the density of the desorbed plume remains elevated for longer periods due to the one-dimensional expansion. However, in the case of nanowires and quantum dots, the expansion of the plume is three-dimensional.²⁸ The different plume dimensionalities result in altered plume reactions, between the plume and surface and within the plume.

In-plume collisions and secondary ion–molecule reactions are highly dependent on the plume dynamics.

In metallic structures, the absorption of photons can also result in the emission of electrons *via* the photoelectric effect. Ion yields from very thin layers of sample in MALDI experiments are shown to change depending on the work function of the target plate material, indicating the role of electron emission.¹⁴⁰ Such effects are absent in the case of thicker samples.¹⁴¹ The emitted electrons can react in the plume and produce more negatively charged species, decrease the number of positively charged species, or produce more fragment ions *via* electron impact. Enhanced electron emission was observed on biased silicon surfaces microstructured at sub-bandgap wavelengths.¹⁴² The combination of these observations points to the potential role of the enhanced photoelectron emission from some of the nanostructures in altering the ion yields.

Except in the case of preformed ions, the source of protons in matrix-free LDI experiments is unclear. Protons may come from residual solvent molecules, surface functional groups, or the adsorbate itself. The solvent and surface effects have been studied in DIOS¹⁴³ and LISMA⁴³ using deuterated reagents and surface derivatization to determine the source of protons. In the DIOS studies, the solvents with low proton affinity and vapor pressures showed to be better proton donors, and more acidic surface functional groups resulted in improved signal.

In LDI experiments from LISMA, exclusively protonated molecular ions were observed when the microcolumn structures were produced in D₂O rather than H₂O, whereas using D₂O solvent for the deposition of the adsorbates instead of H₂O resulted in deuterated molecules in the mass spectra. These results seem to indicate that the role of the surface functional groups in LDI from LISMA is minimal and the residual solvent molecules act as the source of protons.⁴³ However, when the concentration of surface hydroxides on the LISMA was increased by raising the pH of the processing environment, the ionization process became more efficient.¹⁴⁴ This implied that surface chemistry also played a role in LDI from LISMA.

On structured silicon substrates, interactions with surface functional groups, specifically hydrogen bonds, were shown to participate in the chemical reactions with the adsorbate.¹²⁹ These experiments also showed that the proton affinity of the adsorbate might govern the ionization efficiency. In other surface assisted methods, the acidity of surface interface layers was found to be important.¹⁴⁵ In the studied methods, the origin of protons can be traced to both the surface groups and the residual solvent molecules.

The dissociation of molecular ions is governed by the excess internal energy transferred to the ions during and after the laser pulse. In some matrix-free soft ionization techniques, *e.g.*, DIOS and SiNW, the internal energies of the desorbed ions are independent of the laser fluence.^{28,139} To enhance the fragmentation of some adsorbates (for example, peptides), often a second ion activation step, such as collisions with a background gas, is needed. LDI from gold nanoparticles results in fragmentation of molecular ions as well as gold clusters; however, in these experiments the fragmentation is not controlled.¹²⁰ In contrast, the desorption and ionization of peptide ions from LISMA and NAPA substrates results in the formation of molecular ions at low laser fluences followed by

the emergence of structure-specific fragment ions as the laser fluence increases.^{42,44} The fragment ions are produced through both high- and low energy decomposition channels and the fragmentation pathways have many similarities with surface-induced dissociation. Furthermore, the desorption and fragmentation of ions is dependent on the plane of polarization of the desorption laser.^{20,133} The enhanced fields around high aspect ratio posts, energy confinement in thin posts, surface-adsorbate collisions, and reactive fragmentation channels are all thought to contribute to molecular fragmentation from NAPA. The ability to control the degree of fragmentation is useful for molecular identification and structure elucidation of adsorbate molecules.

3 Applications

3.1 Figures of merit for photonic ion production

From the point of view of applications, the initial appeal of using nanostructures to facilitate ionization for MS was the elimination of matrix interferences, endemic in MALDI, in the low mass range. It was also anticipated that nanostructured substrates would result in increased sensitivity due to the better signal-to-noise ratio, improved control over fragmentation, and, with nanofabrication, the ability to optimize ion production. Current experience with these ionization platforms, however, paints a varied picture of their performance.

In mass spectrometric applications, simplified sample preparation, minimized interferences, and increased sensitivity afforded

by the nanostructure-based ionization platforms are essential. For example, Fig. 4a shows that with DIOS an ultralow detection limit of 800 yoctomoles can be achieved, *i.e.*, ~480 molecules can be detected.²³ This is the result of high ion yields from these surfaces, as well as the dramatically reduced background in the low mass range due to the lack of matrix-related ions. An additional advantage of the matrix-free approach is that no chemical compatibility of matrix and analyte is needed. It is worth noting that some nanoparticle systems require the use of surfactants, additives or surface modifiers that can also obscure the low mass region.

Mesoscopic and nanostructured materials, such as LISMA,²⁴ NAPA,⁴⁴ DIOS,¹⁴⁶ the substrate used in nanostructure initiator mass spectrometry (NIMS),¹⁴⁷ GALDI,³⁷ nanorods,¹²¹ and nanowells,¹⁴⁸ at adsorbate ion generation fluences do not undergo substantial morphological transformation. Surface derivatization, including hydrosilylation,²¹ can further improve substrate stability and reusability. In addition, as shown in Fig. 4b for verapamil as the analyte, substrates with improved stability, *e.g.*, LISMA, can provide a wide dynamic range for quantitation.

When certain nanostructures, such as gold nanofilms,³² are exposed to high laser fluences, ionized clusters of the substrate can cause interferences.¹²³ Thus, keeping the laser fluence close to the analyte ion generation threshold improves the quality of the mass spectra. Nanodots, composed of various semiconductors and metal oxides, have been developed to improve the limits of detection for small organic molecules and peptides.

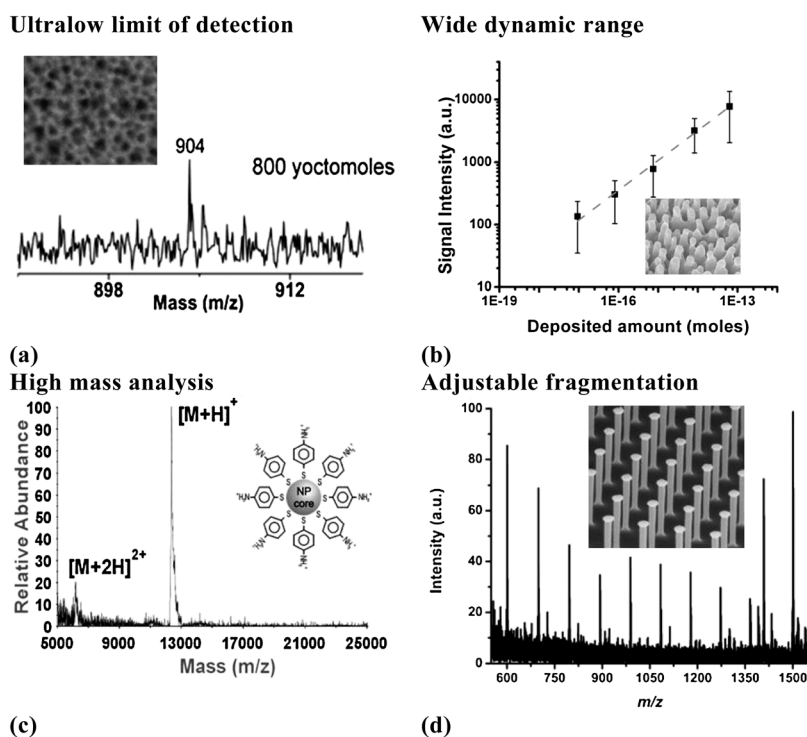


Fig. 4 LDI-MS from various nanostructures. (a) An 800 yoctomole limit of detection was demonstrated on a DIOS platform. Reprinted with permission from ref. 23. Copyright [2004], American Chemical Society. Image in the inset is reprinted with permission from ref. 22. Copyright [2010], Elsevier. (b) LISMA exhibits a dynamic range of 5 orders of magnitude and a limit of detection of 8 amoles for verapamil. (c) Large peptides, such as cytochrome *c*, are detected from derivatized gold nanoparticles. Reprinted with permission from ref. 149. Copyright [2007], American Chemical Society. (d) Structure specific fragmentation of the synthetic peptide P14R from derivatized NAPA was obtained by increasing the laser fluence. Sodiated a- and c-type fragment ions are observed.²⁰

For example, self-assembled germanium nanodots, grown on silicon substrates, exhibited low detection limits (800 amol for angiotensin I and 200 fmol for insulin) along with the ability to detect small molecules.³⁵

Another important figure of merit for matrix-free ion production is the high mass limit characterized by the decline of efficient ionization. In the past few years, extensive efforts were made to improve the detection of large molecules using nanoparticles (see Fig. 4c),¹⁴⁹ nanowells,¹⁴⁸ or closely packed nanotube arrays¹⁵⁰ with diameters of ~ 200 nm. Nanotube arrays have shown a high mass limit of ~ 29 kDa and are robust enough to withstand high laser fluences. However, for small molecules the limit of detection is somewhat disappointing (~ 6 fmol), making this ionization platform less suitable for trace analysis. It has also been demonstrated that CdS quantum dots, with particle sizes between 1 nm and 10 nm, can be used to detect large proteins with molecular weights from 5–80 kDa, including bovine serum albumin (molecular weight 66.0 kDa) and human apo-transferrin (molecular weight 79.8 kDa).¹⁵¹ These quantum dots, however, seem to ablate with the adsorbate, acting as a pseudo-matrix.

Gold nanorods,¹²¹ with longitudinal surface plasmon resonance modes that are commensurate with the wavelength of the desorption laser, efficiently desorb and ionize small biomolecules but are not suitable for the detection of larger molecules. It was observed that the resonance frequency was influenced by the aspect ratio of the nanorods and, at an aspect ratio of 5, the resonance band overlapped with the Nd:YAG laser wavelength at 1064 nm. Similar to MALDI, these nanoparticles were mixed with the analyte during the preparation steps and deposited together onto a metal substrate. At high laser fluences, Au clusters from the nanorods were desorbed and ionized resulting in spectral interferences. However, in comparison to standard MALDI matrixes like 2,5-dihydroxybenzoic acid and α -cyano-4-hydroxycinnamic acid, these interferences were minor.

Structures with even higher aspect ratios, typically greater than 15, are categorized as nanowires and can be used as efficient ionization platforms. SiNWs are produced by chemical vapor deposition and are typically derivatized with (pentafluorophenyl)-propyldimethylchlorosilane.²⁶ These substrates are the basis of nanowire-assisted LDI commercially available from Bruker Daltonics under the trademarked name of NALDI™. An advantage of SiNWs is a significantly lower ionization fluence threshold compared to MALDI and to other nanostructure-based devices. However, the nanowires are easily melted and evaporated by laser irradiation making shot-to-shot comparisons difficult.²⁸ In addition, they are prone to interferences due to the presence of silicon cluster ions.¹⁵²

Chemical etching is used to produce nanofilms from various metals such as palladium, platinum, and gold. These films usually have a heterogeneous morphology that results in significant shot-to-shot variations in the spectra. Nanofilament substrates can be activated through a dynamic electrowetting process.¹⁵³ Electrowetting results in stronger interactions between the analyte and the nanofilament structure, and improves the limit of detection to a few attomoles.¹⁵⁴

When working with real world samples, both high mass resolution and the production of structure specific fragments

improve the identification accuracy for unknown molecules. Substantially increasing the laser fluence has been shown to induce analyte fragmentation.⁴² At elevated fluences, robust structures, *e.g.*, LISMA⁴² and NAPA,⁴³ have been demonstrated to induce structure specific fragmentation without the use of collision activated dissociation, electron capture dissociation, or other activation methods (see Fig. 4d). These structures enable a new approach to the structural characterization of small organic molecules and peptides. Additional efforts to understand the interaction of laser radiation with nanophotonic structures at elevated intensities can lead to the development of new ways to induce structure specific ion fragmentation.

Nanoparticles such as TiO₂,⁴⁰ Ag,¹⁵⁵ and Au¹⁵⁶ can be modified with surface ligands that can selectively bind to a particular type of molecule. These selective capturing agents increase the specificity and selectivity of the LDI analysis. When these nanoparticles are irradiated with the laser, the surface ligands are detached from the core and become ionized. These derivatized nanoparticles are envisioned for imaging, protein recognition, and clinical diagnostics applications.¹⁵⁷ In other cases, various molecular caps have been added to gold nanorods to selectively target molecules that have an affinity to the capping agent.¹²¹

Quasi-periodic nanostructures, such as nanowells¹⁴⁸ and nanocavities,¹⁵⁸ exhibit characteristics comparable to LISMA and DIOS. Nanocavities can be produced by oxidizing a silicon wafer and convectively assembling SiO₂ beads to the surface. The structures are then processed *via* reactive ion etching and cavities are created where the SiO₂ beads do not cover the surface. By systematically varying the size of cavities, it was established that signal-to-noise ratios for the mass spectra exhibited a minimum at a particular surface roughness.

In order to better understand the laser–nanostructure interactions, systems with dimensions tailored in a broad range are necessary. Nanofabrication protocols with sufficient control over the array geometries can be developed to systematically tune the interaction between the structures and the laser radiation for optimum ion production. Ordered monolithic silicon structures such as NAPA,⁴⁴ nanocavity arrays,⁴⁵ and nanotips⁴⁶ are examples of such mechanistic studies. Cylindrical NAPA fabricated with systematically varied heights, diameters, and periodicities showed up to a 55-fold improvement in ion yields when for a given post diameter the optimum aspect ratio was found.⁴⁴

Systematic studies on nanocavity arrays indicated that when the porosity of nanocavities increased, the fluence threshold required to obtain ion signal decreased.⁴⁵ Nanocavities with porosities similar to DIOS were found to have the lowest fluence threshold as well as the greatest ionization efficiency. Furthermore, deeper nanocavities (459 nm) exhibited lower laser fluence thresholds than structures with shallower cavities (200 nm). Similarly, silicon nanowell arrays demonstrated a 100-fold increase in ionization efficiency when well depths increased from 10 nm to 50 nm.¹⁴⁸

Desorption and ionization from silicon nanotip arrays (DIOSTA) is another example of ordered monolithic structures used for LDI. Following the techniques used to create electron field emitters, DIOSTA were produced with tip diameters as small as 10 nm.⁴⁶ These nanotip arrays were used for ion production

from low mass peptides and other biomolecules, including dopamine, with moderate limits of detection in the low picomole range. Systematically exploring the parameter space for the geometry of these devices could significantly improve the ion yields and consequently the analytical performance.

3.2 Amenable sample types

Following the success of MALDI-MS for the analysis of proteins and peptides, the need for a laser-based method for small molecules became apparent. Due to the overwhelming spectral interferences from the matrix ions in the low mass region ($m/z < 500$), important classes of compounds and applications remained intractable, initiating a quest for a 'matrix-free' laser ionization technique. It was quickly recognized that nanostructures held the potential to utilize laser energy for the desorption and ionization of pharmaceuticals, metabolites, peptides, lipids and xenobiotics, as well as their complex mixtures. In this section we discuss specific applications of nanostructures used in the mass spectrometric analysis of various sample types.

Metabolites and xenobiotics. Metabolites are the intrinsic molecular building blocks of biological systems, whereas xenobiotics are extraneous molecules introduced from the environment. The vast structural diversity of these chemical species makes it difficult to find a universal technique for their efficient ionization. Due to the complexity of biological samples, minimizing interferences, improving sensitivity and selectivity, and exhibiting a wide dynamic range are critical. Nanostructure-based ionization methods can meet several of these challenges.

With the proper selection of the initiator molecule in negative mode NIMS, trace level detection of phosphorylated metabolites associated with energy transport (adenosine 5'-triphosphate (ATP), adenosine 5'-diphosphate (ADP) and guanosine 5'-triphosphate (GTP)) was achieved.¹⁵⁹ Oxidized DIOS structures appear to efficiently aid the laser ionization of catecholamines, important neurotransmitters, and other metabolites extracted from lymphocytes.¹⁶⁰

In the analysis of small biomolecules, laser ionization from silicon nanopowder substrates offers improved sensitivity, reduced interferences, and expanded coverage of trace components, *e.g.*, xenobiotics in urine (see Fig. 5a).¹⁶¹ Due to the homogeneous distribution of the nanopowder-sample mixture, this technique offers improved reproducibility and semi-quantitation.

Trace components, such as resveratrol, in highly complex samples, *e.g.*, red wine, have been linked to beneficial health effects. However, the average concentrations of resveratrol in wine are low (2–10 μM) and the conventional mass spectra of these samples are complex, usually resulting in the need for a separation step. Fig. 5b shows that laser irradiation of a wine sample on NAPA efficiently ionizes the resveratrol without the need for extraction.

Peptides. Model peptides and their simple mixtures are commonly utilized to demonstrate the analytical figures of merit of new ionization methods in the low to medium mass range.¹⁴⁷ Biologically relevant peptide-containing samples (microorganisms, tissues, *etc.*), however, are highly complex. Laser ionization from nanostructures can be used for the analysis of these complex specimens. Direct mass spectrometric analysis

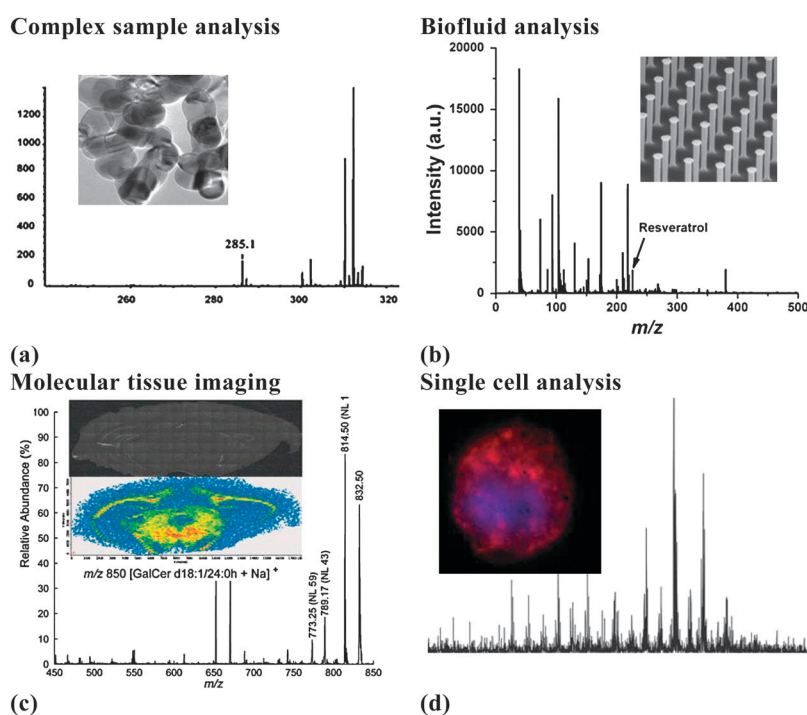


Fig. 5 Selected applications of laser desorption ionization sources based on nanostructures. (a) The analysis of morphine in biofluids using silicon nanopowder. Reprinted with permission from ref. 161. Copyright [2007], American Chemical Society. (b) Direct analysis of white wine using NAPA shows the presence of resveratrol. (c) Imaging and identification of glycolipid species from rat brain tissue with GALDI. Reprinted with permission from ref. 37. Copyright [2007], American Chemical Society. (d) Direct analysis of a single cancer cell with NIMS. Reprinted with permission from ref. 147. Copyright [2007], Nature Publishing Group.

of several neuropeptides from exocrine tissue, single neurons, and the atrial gland of *Aplysia californica* was achieved with DIOS in the 1000–4000 Da mass range.¹⁶² Similarly, inorganic nanoparticles were used to promote the laser ionization of peptides under 1500 Da in rat cerebellar sections for MS imaging with lateral resolution of 15 μm .¹⁶³

The ability to promote peptide fragmentation on nanostructures offers advantages in the elucidation of their structure. The ability to generate peptide fragments has been demonstrated for, e.g., LISMA,²⁴ NAPA²⁰ and capped gold nanoparticles.¹⁶⁴ Methods to promote fragmentation included surface modifications,¹³⁹ increasing the laser fluence,^{20,42} and varying the polarization angle of the laser beam.²⁰

Carbohydrates. Carbohydrates are omnipresent in biologically relevant substances but are not always amenable to ion production by conventional laser-based methods. The ionization of carbohydrates is inefficient because they lack basic or acidic groups that promote protonation and deprotonation. Laser ionization on nanostructures offers alternative ionization pathways through the formation of Na^+ and K^+ adducts with appreciable yield.

Reported examples include the detection of carbohydrates in biofluids and tissues¹⁶⁵ and proteolytic digests¹⁶⁶ by NIMS. Other nanostructures successfully used for the laser ionization of carbohydrates include nanoparticles, e.g., gold¹⁶⁷ and titanium oxide,¹⁶⁸ and platinum nanoflowers.¹⁶⁹

Pharmaceuticals. Pharmaceutical research relies on ion production for MS during the development and synthesis of drug candidates, as well as in studying their absorption, distribution, metabolism and excretion (ADME) in various organisms. To improve their bioavailability, the molecular weights of most pharmaceuticals are below 1000 Da, making them amenable for nanostructure-based LDI. These ion sources are particularly fitting for pharmaceutical analysis due to the minimal interference from substrate-related ions observed in the low mass range.¹⁷⁰

Quantitative response¹⁷¹ and selective capture¹⁷² of drug molecules from complex mixtures have been shown using DIOS with the prospect of affinity purification on a chip for the latter. Other nanostructures, such as nanofilms,¹⁷³ graphite¹⁷⁴ and silicon nitride nanoparticles,¹⁷⁰ LISMA,²⁴ and NAPA⁴⁴ have also been utilized for the analysis of pharmaceuticals with ultra-low limits of detection, e.g., 6 attomoles of verapamil for the latter.

Once administered, the metabolized drugs can be analyzed from various biofluids, e.g., blood serum¹⁴⁷ and urine,¹⁷⁵ as well as from tissues. In one such example, LDI from TiO_2 nanoparticles was used to detect metabolized pharmaceuticals, such as the hypertension drug propranolol, in urine. Indicator metabolites, for example, testosterone, can also be monitored to verify the delivery of an ingested drug.¹⁷⁵

Forensic samples. Low limits of detection and short analysis times have motivated the application of nanostructure-based LDI MS to forensically relevant small molecules such as drugs of abuse,^{171,176–178} certain xenobiotics^{179,180} and explosives.¹⁸¹

A growing number of examples indicate the potential of nanostructures in the LDI of illicit drugs. Using SiNWs, cocaine, along with one of its metabolites, were detected in human serum.²⁶

In LDI-MS experiments, dusting agents containing carbon black nanoparticles, used to visualize latent fingerprints, proved efficient in detecting the presence of drugs of abuse in the prints.¹⁷⁸ DIOS-MS showed promising performance in the rapid quantitation of codein,¹⁷¹ and in some cases, e.g., for 3,4-methylenedioxymethamphetamine (Ecstasy), the impurity profile of the drug could be determined to identify the producer or reveal potentially lethal contaminants.¹⁸² The specificity of detecting a particular component in the presence of multiple drugs can be improved by combining its immunocapture on the nanostructure with LDI-MS.¹⁷⁶

In criminal investigations, trace amounts of synthetic polymers from contraceptives were detected in physical evidence by DIOS-MS.^{179,180} This is probably the first example of nanostructure-based LDI-MS of evidence admitted in court.

The detection of high explosives, e.g., tetryl, was also demonstrated on meso-structured porous polymer monoliths.¹⁸¹ These synthetic polymer substrates offer better air stability than the porous silicon in DIOS enabling their long term storage.

Environmental samples. The efficacy of nanostructures for LDI-MS of environmental contaminants, including harmful organic compounds as well as microbial pollutants, is tested in various laboratories. To gauge the success of remediation, trace detection of the contaminants is necessary, making high ionization efficiency essential.

A pyrolytic graphite polymer film¹⁸³ and DIOS¹⁸⁴ were used for the ultrasensitive detection of perfluorooctanoic acid, perfluorooctane sulfonate, bisphenol A, pentachlorophenol, and other industrial pollutants. A large variety of environmental contaminants showed a strong ion signal when oxidized carbon nanotubes were used as LDI substrates.¹⁸⁵

In a recent study, the detection of highly infectious bacteria in air, on human skin, and in nasal passages was demonstrated.¹⁸⁶ Due to the high sensitivity of LDI-MS using TiO_2 nanoparticles, the time consuming culturing step involved in the traditional method of detecting *Staphylococcus aureus* (“Staph”) infection could be eliminated. The resulting MS-based biosensor is a faster (a few minutes compared to 48 hours) and more sensitive approach to “Staph” detection.

Tissue imaging. Publications on MS imaging of tissues have increased exponentially since the emergence of MALDI-based methods in 1997.¹⁸⁷ There are two approaches to establish MS imaging of tissues based on LDI from nanostructures. First, nanoparticles can be deposited on the tissue surface in a way similar to the application of a conventional matrix. In the second approach, a thin tissue section can be deposited on top of a nanostructure. In both cases the laser pulses excite the surface pixel-by-pixel and mass spectra are collected from every spot. The distributions of the various chemical species on the surface can be visualized by representing the intensity of the corresponding ion peak in the mass spectra for every pixel on a false-color scale.

Due to the superior limits of detection and dramatically reduced interferences in the low mass range compared to MALDI, nanostructure-based MS imaging is more suitable for exploring metabolite and lipid distributions in tissues. In an example of the first approach, colloidal graphite with a

typical particle size of 1 μm was sprayed on rat brain tissue sections. This imaging GALDI technique captured the distributions of some glycolipids (cerebrosides and sulfatides) in the section (see Fig. 5c).³⁷

The second approach is best represented by NIMS^{147,165} and NALDI¹⁸⁸ imaging studies. Distribution of lipids in and around the spinal cord of a mouse embryo was mapped by NIMS from a tissue section.¹⁴⁷ To enhance the ionization of carbohydrates and steroids, sodium and silver salts, respectively, were deposited on the porous silicon surface. Distributions of sucrose in a flower stem and cholesterol in a mouse brain section were observed.¹⁶⁵ Using commercially available NALDI structures, LDI-MS imaging of lipids in mouse kidney samples indicated the ability to chemically distinguish between the adrenal gland and the kidney tissue.¹⁸⁸

Single cell analysis. Understanding the nature and biological role of cellular heterogeneity, the biochemical differences between individual cells, promises new insights into how cellular systems grow, develop, and interact with their environment. The extremely small volume of cells (the volume of a yeast cell is typically ~ 30 fL) and their compositional complexity (thousands of metabolites, lipids and proteins) make this task challenging.

Based on the biomass composition of *Saccharomyces cerevisiae*,¹⁸⁹ in order to detect abundant components like alanine and uridine 5'-monophosphate (UMP) from a single cell, limits of detection of at least 32 fmol and 4 fmol, respectively, are required. However, to detect a less abundant metabolite, for example ergosterol, a detection limit of 70 amol is necessary. As MALDI-MS typically exhibits ~ 1 fmol limit of detection, it is able to detect alanine and UMP but not ergosterol in a single yeast cell. However, LISMA, with limits of detection in the low attomoles and a wide dynamic range, could detect ergosterol and other less, as well as more abundant metabolites resulting in richer, more informative spectra.

Direct LDI-MS analysis of single cells deposited intact on a nanostructure can simplify sample preparation, minimize interferences from matrixes, and reduce contamination. Fig. 5d shows how NIMS can be used to generate a mass spectrum from a single metastatic breast cancer cell.¹⁴⁷ Repeating such measurements for cells of different genotypes or phenotypes can reveal compositional differences stemming from cellular heterogeneity.

Continued research involving the direct analysis of small cell populations and single cells can lead to a better knowledge of their biochemical functioning. Due to the commensurability of nanostructures and cells—that are biological nanostructures themselves—manipulation and analysis of individual cells on these platforms promise to be a rich area of research.

4 Outlook

Pulsed laser excitation of nanostructures above a certain fluence gives rise to ion production from organic and biomolecular adsorbates. In many cases, the associated phenomena rely on modified optical, electronic, and thermal properties due to nanoscopic structuring. Enhancement of the excitation field in the proximity of the surface, various confinement effects, plasmon resonances, in-plume reactions, and adsorbate–solvent and adsorbate–surface interactions may all affect the mechanism of desorption, ionization, and fragmentation.

Many of these phenomena can be derived from photonic interactions. They result in a new method of producing ions that we have termed photonic ionization. The unique properties associated with the corresponding devices, *i.e.*, photonic ion sources, include polarization dependent ion yields and fragmentation, as well as ion yield resonances at particular aspect ratios of the nanoscopic features.

Accumulating evidence points to the role the relationship between the characteristic lengths of transport processes and the critical dimensions of the nanostructures plays in ion production. The confinement of energy, charge or plume material that occurs when a characteristic length exceeds the critical dimension of the structure can all be important in the underlying ionization mechanisms. With a growing understanding of the mechanisms, there is an increasing possibility of rational nanostructure design for the production of ions.

Chemical modification of the surface to either selectively capture certain adsorbate types or to enhance the desorption ionization yields can also have a major impact on the performance of photonic ion sources. Powerful examples include the capping of nanoparticles with organics to extend the high mass range of these ion sources. The modification of the substrate, *via* chemical derivatization, can decrease the adsorbate–surface interaction thus increasing the rate of desorbing and ionizing intact molecules. Introducing protons from the surface or from trapped solvent can result in more efficient ionization. Ultimately, ion production from large adsorbates ($m/z > 10\,000$) is very efficient through conventional MALDI, so there is less motivation for the use of nanostructures in that mass range. Therefore, it is more likely that surface modification will find a use in lowering the limit of detection and controlling the internal energy of the produced ions.

The ability to control ion decomposition levels from no or little fragmentation to the production of structure-specific fragments through adjusting the laser fluence, incidence angle, or polarization is a feature unique to some nanostructures. This property offers a yet unutilized approach to structure exploration in MS. Currently, complex methods and extra instrumentation are used to induce controllable fragmentation in organic and biomolecules. These techniques include collision induced dissociation, surface induced dissociation and photodissociation, in combination with tandem mass spectrometers. Manipulating the fluence and the plane of polarization in photonic ion sources offers a simpler approach, potentially with a single stage mass spectrometer. Analytical applications of nanostructured ionization platforms benefit from ultra-low limits of detection with a wide dynamic range. Tailoring the dimensions of these structures through nanofabrication has shown that major improvements can be achieved in the ion yields due to resonant behavior, *e.g.*, at certain aspect ratios for NAPA. Similar resonances are expected for plasmonic structures with concomitant drop in the limit of detection. A greater understanding of the essential factors, contributing to the laser desorption and ionization mechanisms in these systems, will allow for the optimization of the nanostructure dimensions for efficient ion production. As a result, the application of nanostructured ionization platforms could be extended from metabolomics to other classes of biomolecules.

Limitations of the nanostructure-based approach to LDI include the need for robust production of the structures themselves.

To achieve high ion yields and low background levels, the ultimate preparation of these platforms will probably include nanofabrication.

Primary metabolites in single cells are present at the low femtomole levels. With certain nanostructures exhibiting limits of detection in the zeptomoles to yoctomoles range, they are prime candidates for the panoramic metabolic analysis of single cells. This fast growing field promises new insights into cellular heterogeneity and related biological phenomena. Integration of the culturing and manipulation of cells on these nanostructured platforms can also be achieved by common nanofabrication procedures.¹⁹⁰

With the advent of ambient ion sources, there is growing interest in shifting the use of nanostructured LDI platforms from vacuum to atmospheric pressure.^{148,191} With a large surface area in these systems exposed to laser excitation, oxygen and humidity in the ambient environment, chemical stability is expected to be a significant issue. Despite the technical difficulties in creating a sufficiently stable LDI substrate, the promise of minimal sample preparation and the ability to directly analyze functioning cells can provide sufficient incentive to pursue their development.

Combining separation with ion production in nanostructured systems promises enhanced capabilities. For example, due to the unique adsorbate–surface interactions on SiNWs, molecules in a complex mixture can be separated to different regions of the structure followed by LDI of the separated components.¹³² Other strategies include substrate-selective binding for the capture of a target molecule. Selective capture by nanostructured platforms is a promising tool for the analysis of the enzymatic digest products of proteins and for the cleanup of complex samples.^{23,121,192} Altering the surface chemistry of the nanostructures can promote selective capture of certain molecules and improve the sensitivity by their accumulation on the surface.

Utilizing the interactions of photonic structures with laser radiation for ion production is beginning to take off. The small size of these versatile multifunctional ionization platforms makes them good candidates for the integration with miniaturized mass spectrometers. Understanding the underlying principles of ion production by nanostructures paves the way for their rational design and integration into complex analytical systems.

Acknowledgements

The authors are grateful for the financial support from the Chemical Sciences, Geosciences and Biosciences Division within the Office of Basic Energy Sciences of the U.S. Department of Energy (DE-FG02-01ER15129) and from Protea Biosciences, Inc. Support from the Department of Energy does not constitute an endorsement of the views expressed in the article. Funding by the George Washington University Selective Excellence Funds and scholarships from the Achievement Rewards for College Scientists Foundation, Inc., (ARCS) to J.A.S. and B.N.W. are also acknowledged.

Notes and references

- 1 K. W. H. Tanaka, Y. Ido, S. Akita, Y. Yoshida and T. Yoshida, *Rapid Commun. Mass Spectrom.*, 1988, **2**, 151–153.
- 2 M. Karas and F. Hillenkamp, *Anal. Chem.*, 1988, **60**, 2299–2301.
- 3 K. Dreisewerd, *Chem. Rev.*, 2003, **103**, 395–425.
- 4 A. Meffert and J. Grotemeyer, *Isr. J. Chem.*, 2001, **41**, 79–90.
- 5 A. Vertes, G. Irinyi and R. Gijbels, *Anal. Chem.*, 1993, **65**, 2389–2393.
- 6 X. W. Wu, M. Sadeghi and A. Vertes, *J. Phys. Chem. B*, 1998, **102**, 4770–4778.
- 7 M. Sadeghi, X. W. Wu and A. Vertes, *J. Phys. Chem. B*, 2001, **105**, 2578–2587.
- 8 R. Knochenmuss, *Anal. Chem.*, 2003, **75**, 2199–2207.
- 9 R. Knochenmuss and R. Zenobi, *Chem. Rev.*, 2003, **103**, 441–452.
- 10 R. Knochenmuss, *J. Mass Spectrom.*, 2002, **37**, 867–877.
- 11 M. Sadeghi and A. Vertes, *Appl. Surf. Sci.*, 1998, **127–129**, 226–234.
- 12 F. Gamez, P. Hurtado, P. M. Castillo, C. Caro, A. R. Hortal, P. Zaderenko and B. Martinez-Haya, *Plasmonics*, 2010, **5**, 125–133.
- 13 D. G. Cahill, K. Goodson and A. Majumdar, *J. Heat Transfer*, 2002, **124**, 223–241.
- 14 S. Eustis and M. A. El-Sayed, *Chem. Soc. Rev.*, 2006, **35**, 209–217.
- 15 M. von Allmen and A. Blatter, *Laser-beam interactions with materials physical principles and applications*, Springer-Verlag, 1995.
- 16 S. R. Scully and M. D. McGehee, *J. Appl. Phys.*, 2006, **100**, 093521.
- 17 P. D. Setz and R. Knochenmuss, *J. Phys. Chem. A*, 2005, **109**, 4030–4037.
- 18 A. A. Joshi and A. Majumdar, *J. Appl. Phys.*, 1993, **74**, 31–39.
- 19 T. Yonezawa, H. Kawasaki, A. Tarui, T. Watanabe, R. Arakawa, T. Shimada and F. Mafune, *Anal. Sci.*, 2009, **25**, 339–346.
- 20 J. A. Stolee and A. Vertes, *Phys. Chem. Chem. Phys.*, 2011, **13**, 9140–9146.
- 21 J. Wei, J. M. Buriak and G. Siuzdak, *Nature*, 1999, **399**, 243–246.
- 22 K. P. Law, *Int. J. Mass Spectrom.*, 2010, **290**, 72–84.
- 23 S. A. Trauger, E. P. Go, Z. X. Shen, J. V. Apon, B. J. Compton, E. S. P. Bouvier, M. G. Finn and G. Siuzdak, *Anal. Chem.*, 2004, **76**, 4484–4489.
- 24 Y. Chen and A. Vertes, *Anal. Chem.*, 2006, **78**, 5835–5844.
- 25 C. K. Chiang, N. C. Chiang, Z. H. Lin, G. Y. Lan, Y. W. Lin and H. T. Chang, *J. Am. Soc. Mass Spectrom.*, 2010, **21**, 1204–1207.
- 26 E. P. Go, J. V. Apon, G. Luo, A. Saghatelian, R. H. Daniels, V. Sahi, R. Dubrow, B. F. Cravatt, A. Vertes and G. Siuzdak, *Anal. Chem.*, 2005, **77**, 1641–1646.
- 27 K. P. Law, *Int. J. Mass Spectrom.*, 2010, **290**, 47–59.
- 28 G. H. Luo, Y. Chen, H. Daniels, R. Dubrow and A. Vertes, *J. Phys. Chem. B*, 2006, **110**, 13381–13386.
- 29 L. Colaianni, S. C. Kung, D. K. Taggart, V. De Giorgio, J. Greaves, R. M. Penner and N. Cioffi, *Sens. Lett.*, 2010, **8**, 539–544.
- 30 G. Piret, H. Drobecq, Y. Coffinier, O. Melnyk and R. Boukherroub, *Langmuir*, 2010, **26**, 1354–1361.
- 31 S. Dagan, Y. M. Hua, D. J. Boday, A. Somogyi, R. J. Wysocki and V. H. Wysocki, *Int. J. Mass Spectrom.*, 2009, **283**, 200–205.
- 32 R. Nayak and D. R. Knapp, *Anal. Chem.*, 2010, **82**, 7772–7778.
- 33 V. Jokinen, S. Aura, L. Luosjarvi, L. Sainiemi, T. Kotiaho, S. Franssila and M. Baumann, *J. Am. Soc. Mass Spectrom.*, 2009, **20**, 1723–1730.
- 34 A. L. Pyayt, B. Wiley, Y. N. Xia, A. Chen and L. Dalton, *Nat. Nanotechnol.*, 2008, **3**, 660–665.
- 35 T. Seino, H. Sato, A. Yamamoto, A. Nemoto, M. Torimura and H. Tao, *Anal. Chem.*, 2007, **79**, 4827–4832.
- 36 H. Sato, A. Nemoto, A. Yamamoto and H. Tao, *Rapid Commun. Mass Spectrom.*, 2009, **23**, 603–610.
- 37 S. W. Cha and E. S. Yeung, *Anal. Chem.*, 2007, **79**, 2373–2385.
- 38 H. Kawasaki, T. Yonezawa, T. Watanabe and R. Arakawa, *J. Phys. Chem. C*, 2007, **111**, 16278–16283.
- 39 J. Sunner, E. Dratz and Y. C. Chen, *Anal. Chem.*, 1995, **67**, 4335–4342.
- 40 C. T. Chen and Y. C. Chen, *Anal. Chem.*, 2005, **77**, 5912–5919.
- 41 S. W. Cha, H. Zhang, H. I. Ilarslan, E. S. Wurtele, L. Brachova, B. J. Nikolau and E. S. Yeung, *Plant J.*, 2008, **55**, 348–360.
- 42 J. A. Stolee, Y. Chen and A. Vertes, *J. Phys. Chem. C*, 2010, **114**, 5574–5581.
- 43 J. A. Stolee, B. N. Walker, Y. Chen and A. Vertes, *AIP Conf. Proc.*, 2010, **1278**, 98–110.
- 44 B. N. Walker, J. A. Stolee, D. L. Pickel, S. T. Retterer and A. Vertes, *J. Phys. Chem. C*, 2010, **114**, 4835–4840.

- 45 Y. S. Xiao, S. T. Retterer, D. K. Thomas, J. Y. Tao and L. He, *J. Phys. Chem. C*, 2009, **113**, 3076–3083.
- 46 A. Gorecka-Drzazga, J. Dziuban, W. Drzazga, A. Kraj and J. Silberring, *J. Vac. Sci. Technol. B*, 2005, **23**, 819–823.
- 47 J. Z. Zhang *Optical Properties and Spectroscopy of Nanomaterials*, World Scientific Publishing Co. Pte. Ltd., Singapore, 2009, ch. 5, pp. 117–180.
- 48 K. Ujihara, *J. Appl. Phys.*, 1972, **43**, 2376–2383.
- 49 P. W. Chan, Y. W. Chan and H. S. Ng, *Phys. Lett. A*, 1977, **61**, 151–153.
- 50 C. V. Shank, R. Yen and C. Hirlimann, *Phys. Rev. Lett.*, 1983, **50**, 454–457.
- 51 P. Taneja, P. Ayyub and R. Chandra, *Phys. Rev. B: Condens. Matter Mater. Phys.*, 2002, **65**, 245412.
- 52 Y. F. Huang, S. Chattopadhyay, Y. J. Jen, C. Y. Peng, T. A. Liu, Y. K. Hsu, C. L. Pan, H. C. Lo, C. H. Hsu, Y. H. Chang, C. S. Lee, K. H. Chen and L. C. Chen, *Nat. Nanotechnol.*, 2007, **2**, 770–774.
- 53 T. Shegai, Z. P. Li, T. Dadosh, Z. Y. Zhang, H. X. Xu and G. Haran, *Proc. Natl. Acad. Sci. U. S. A.*, 2008, **105**, 16448–16453.
- 54 Z. P. Li, T. Shegai, G. Haran and H. X. Xu, *ACS Nano*, 2009, **3**, 637–642.
- 55 C. H. Crouch, J. E. Carey, J. M. Warrender, M. J. Aziz, E. Mazur and F. Y. Genin, *Appl. Phys. Lett.*, 2004, **84**, 1850–1852.
- 56 C. Wu, C. H. Crouch, L. Zhao and E. Mazur, *Appl. Phys. Lett.*, 2002, **81**, 1999–2001.
- 57 L. T. Canham, *Appl. Phys. Lett.*, 1990, **57**, 1046–1048.
- 58 A. G. Cullis and L. T. Canham, *Nature*, 1991, **353**, 335–338.
- 59 T. Vanbuuren, Y. Gao, T. Tiedje, J. R. Dahn and B. M. Way, *Appl. Phys. Lett.*, 1992, **60**, 3013–3015.
- 60 I. Sagnes, A. Halimaoui, G. Vincent and P. A. Badoz, *Appl. Phys. Lett.*, 1993, **62**, 1155–1157.
- 61 A. P. Alivisatos, *Science*, 1996, **271**, 933–937.
- 62 J. Perenboom, P. Wyder and F. Meier, *Phys. Rep.*, 1981, **78**, 173–292.
- 63 X. Y. Zhao, C. M. Wei, L. Yang and M. Y. Chou, *Phys. Rev. Lett.*, 2004, **92**, 4.
- 64 C. B. Murray, C. R. Kagan and M. G. Bawendi, *Annu. Rev. Mater. Sci.*, 2000, **30**, 545–610.
- 65 L. Patrono, D. Nelson, V. I. Safarov, M. Sentis, W. Marine and S. Giorgio, *J. Appl. Phys.*, 2000, **87**, 3829–3837.
- 66 J. F. Wang, M. S. Gudiksen, X. F. Duan, Y. Cui and C. M. Lieber, *Science*, 2001, **293**, 1455–1457.
- 67 H. E. Ruda and A. H. Shik, *Phys. Rev. B: Condens. Matter Mater. Phys.*, 2005, **72**, 11.
- 68 J. F. Qi, A. M. Belcher and J. M. White, *Appl. Phys. Lett.*, 2003, **82**, 2616–2618.
- 69 A. Vogel and V. Venugopalan, *Chem. Rev.*, 2003, **103**, 577–644.
- 70 T. Q. Qiu and C. L. Tien, *Int. J. Heat Mass Transfer*, 1992, **35**, 719–726.
- 71 J. Callaway, *Phys. Rev.*, 1959, **113**, 1046.
- 72 M. G. Holland, *Phys. Rev.*, 1963, **132**, 2461.
- 73 D. Y. Li, Y. Y. Wu, P. Kim, L. Shi, P. D. Yang and A. Majumdar, *Appl. Phys. Lett.*, 2003, **83**, 2934–2936.
- 74 X. Lu, J. H. Chu and W. Z. Shen, *J. Appl. Phys.*, 2003, **93**, 1219–1229.
- 75 P. Chantrenne, J. L. Barrat, X. Blase and J. D. Gale, *J. Appl. Phys.*, 2005, **97**, 8.
- 76 S. G. Walkauskas, D. A. Broido, K. Kempa and T. L. Reinecke, *J. Appl. Phys.*, 1999, **85**, 2579–2582.
- 77 S. G. Volz and G. Chen, *Appl. Phys. Lett.*, 1999, **75**, 2056–2058.
- 78 J. Zou and A. Balandin, *J. Appl. Phys.*, 2001, **89**, 2932–2938.
- 79 A. Balandin and K. L. Wang, *Phys. Rev. B: Condens. Matter Mater. Phys.*, 1998, **58**, 1544–1549.
- 80 D. G. Cahill, W. K. Ford, K. E. Goodson, G. D. Mahan, A. Majumdar, H. J. Maris, R. Merlin and S. R. Phillpot, *J. Appl. Phys.*, 2003, **93**, 793–818.
- 81 A. F. Mayadas and M. Shatzkes, *Phys. Rev. B: Solid State*, 1970, **1**, 1382.
- 82 E. H. Sondheimer, *Adv. Phys.*, 2001, **50**, 499–537.
- 83 N. Stojanovic, J. M. Berg, D. H. S. Maithripala and M. Holtz, *Appl. Phys. Lett.*, 2009, **95**, 3.
- 84 N. Stojanovic, D. H. S. Maithripala, J. M. Berg and M. Holtz, *Phys. Rev. B: Condens. Matter Mater. Phys.*, 2010, **82**, 9.
- 85 B. N. Walker, J. A. Stolee, D. L. Pickel, S. T. Retterer and A. Vertes, *Appl. Phys. A: Mater. Sci. Process.*, 2010, **101**, 539–544.
- 86 C. V. Shank, R. Yen and C. Hirlimann, *Phys. Rev. Lett.*, 1983, **51**, 900–902.
- 87 S. Link and M. A. El-Sayed, *Int. Rev. Phys. Chem.*, 2000, **19**, 409–453.
- 88 T. R. Northen, H.-K. Woo, M. T. Northen, A. Nordström, W. Uritboonthail, K. L. Turner and G. Siuzdak, *J. Am. Soc. Mass Spectrom.*, 2007, **18**, 1945–1949.
- 89 J. A. McLean, K. A. Stumpo and D. H. Russell, *J. Am. Chem. Soc.*, 2005, **127**, 5304–5305.
- 90 J. S. Becker, A. Gorbunoff, M. Zoriy, A. Izmer and M. Kayser, *J. Anal. At. Spectrom.*, 2006, **21**, 19–25.
- 91 M. V. Zoriy and J. S. Becker, *Rapid Commun. Mass Spectrom.*, 2009, **23**, 23–30.
- 92 R. Stockle, P. Setz, V. Deckert, T. Lippert, A. Wokaun and R. Zenobi, *Anal. Chem.*, 2001, **73**, 1399–1402.
- 93 T. A. Schmitz, G. Gamez, P. D. Setz, L. Zhu and R. Zenobi, *Anal. Chem.*, 2008, **80**, 6537–6544.
- 94 D. Kossakovski and J. L. Beauchamp, *Anal. Chem.*, 2000, **72**, 4731–4737.
- 95 D. J. Hwang, H. Jeon, C. P. Grigoropoulos, J. Yoo and R. E. Russo, *J. Appl. Phys.*, 2008, **104**, 013110.
- 96 V. Zorba, X. L. Mao and R. E. Russo, *Spectrochim. Acta, Part B*, 2011, **66**, 189–192.
- 97 V. Zorba, X. L. Mao and R. E. Russo, *Appl. Phys. Lett.*, 2009, **95**.
- 98 G. A. Somorjai and M. A. Vanhove, *Prog. Surf. Sci.*, 1989, **30**, 201–231.
- 99 M. L. Wise, B. G. Koehler, P. Gupta, P. A. Coon and S. M. George, *Surf. Sci.*, 1991, **258**, 166–176.
- 100 S. A. Buntin, L. J. Richter, R. R. Cavanagh and D. S. King, *Phys. Rev. Lett.*, 1988, **61**, 1321–1324.
- 101 S. A. Buntin, L. J. Richter, D. S. King and R. R. Cavanagh, *J. Chem. Phys.*, 1989, **91**, 6429–6446.
- 102 J. W. Gadzuk, L. J. Richter, S. A. Buntin, D. S. King and R. R. Cavanagh, *Surf. Sci.*, 1990, **235**, 317–333.
- 103 J. A. Prybyla, H. W. K. Tom and G. D. Aumiller, *Phys. Rev. Lett.*, 1992, **68**, 503–506.
- 104 M. Bonn, S. Funk, C. Hess, D. N. Denzler, C. Stampfl, M. Scheffler, M. Wolf and G. Ertl, *Science*, 1999, **285**, 1042–1045.
- 105 P. Avouris and R. E. Walkup, *Annu. Rev. Phys. Chem.*, 1989, **40**, 173–206.
- 106 R. D. Ramsier and J. T. Yates, *Surf. Sci. Rep.*, 1991, **12**, 243–378.
- 107 R. F. Haglund, in *Laser ablation and desorption*, ed. J. C. Miller and R. F. Haglund, Academic Press, 1998, vol. 30, ch. 2, pp. 15–126.
- 108 A. Vertes, R. Gijbels and R. D. Levine, *Rapid Commun. Mass Spectrom.*, 1990, **4**, 228–233.
- 109 A. Vertes and R. D. Levine, *Chem. Phys. Lett.*, 1990, **171**, 284–290.
- 110 H. F. Hamann, A. Gallagher and D. J. Nesbitt, *Appl. Phys. Lett.*, 2000, **76**, 1953–1955.
- 111 J. N. Farahani, D. W. Pohl, H. J. Eisler and B. Hecht, *Phys. Rev. Lett.*, 2005, **95**, 017402.
- 112 P. Muhlschlegel, H. J. Eisler, O. J. F. Martin, B. Hecht and D. W. Pohl, *Science*, 2005, **308**, 1607–1609.
- 113 E. Cubukcu, E. A. Kort, K. B. Crozier and F. Capasso, *Appl. Phys. Lett.*, 2006, **89**, 093120.
- 114 K. B. Crozier, A. Sundaramurthy, G. S. Kino and C. F. Quate, *J. Appl. Phys.*, 2003, **94**, 4632–4642.
- 115 H. Fischer and O. J. F. Martin, *J. Eur. Opt. Soc.*, 2008, **3**, 08018.
- 116 J. Merlein, M. Kahl, A. Zuschlag, A. Sell, A. Halm, J. Boneberg, P. Leiderer, A. Leitenstorfer and R. Bratschkitsch, *Nat. Photonics*, 2008, **2**, 230–233.
- 117 L. C. Chen, T. Ueda, M. Sagisaka, H. Hori and K. Hiraoka, *J. Phys. Chem. C*, 2007, **111**, 2409–2415.
- 118 L. C. Chen, J. Yonehama, T. Ueda, H. Hori and K. Hiraoka, *J. Mass Spectrom.*, 2007, **42**, 346–353.
- 119 K. Shibamoto, K. Sakata, K. Nagoshi and T. Korenaga, *J. Phys. Chem. C*, 2009, **113**, 17774–17779.
- 120 M. T. Spencer, H. Furutani, S. J. Oldenburg, T. K. Darlington and K. A. Prather, *J. Phys. Chem. C*, 2008, **112**, 4083–4090.
- 121 E. T. Castellana, R. C. Gamez, M. E. Gomez and D. H. Russell, *Langmuir*, 2010, **26**, 6066–6070.

- 122 L. C. Chen, K. Mori, H. Hori and K. Hiraoka, *Int. J. Mass Spectrom.*, 2009, **279**, 41–46.
- 123 K. A. Stumpo and D. H. Russell, *J. Phys. Chem. C*, 2009, **113**, 1641–1647.
- 124 H. B. Huo, M. Y. Shen, S. M. Epstein and H. Guthermann, *J. Mass Spectrom.*, 2011, **46**, 859–864.
- 125 J. N. Anker, W. P. Hall, O. Lyandres, N. C. Shah, J. Zhao and R. P. Van Duyne, *Nat. Mater.*, 2008, **7**, 442–453.
- 126 Y. Nakamura, Y. Tsuru, M. Fujii, Y. Taga, A. Kiya, N. Nakashima and Y. Niidome, *Nanoscale*, 2009, **3**, 3793–3798.
- 127 S. Alimpiev, S. Nikiforov, V. Karavanskii, T. Minton and J. Sunner, *J. Chem. Phys.*, 2001, **115**, 1891–1901.
- 128 G. Piret, H. Drobecq, Y. Coffinier, O. Melnyk and R. Boukherroub, *Langmuir*, 2009, **26**, 1354–1361.
- 129 S. Alimpiev, A. Grechnikov, J. Sunner, V. Karavanskii, Y. Simanovsky, S. Zhabin and S. Nikiforov, *J. Chem. Phys.*, 2008, **128**, 014711.
- 130 Y. Wang, K. Kempa, B. Kimball, J. B. Carlson, G. Benham, W. Z. Li, T. Kempa, J. Rybczynski, A. Herczynski and Z. F. Ren, *Appl. Phys. Lett.*, 2004, **85**, 2607–2609.
- 131 J. L. Bohn, D. J. Nesbitt and A. Gallagher, *J. Opt. Soc. Am. A*, 2001, **18**, 2998–3006.
- 132 E. P. Go, J. V. Apon, G. H. Luo, A. Saghatelian, R. H. Daniels, V. Sahi, R. Dubrow, B. F. Cravatt, A. Vertes and G. Siuzdak, *Anal. Chem.*, 2005, **77**, 1641–1646.
- 133 B. N. Walker, T. Razunguzwa, M. Powell, R. Knochenmuss and A. Vertes, *Angew. Chem., Int. Ed.*, 2009, **48**, 1669–1672.
- 134 P. Kraft, S. Alimpiev, E. Dratz and J. Sunner, *J. Am. Soc. Mass Spectrom.*, 1998, **9**, 912–924.
- 135 R. Gomer, *Surf. Sci.*, 1994, **299**, 129–152.
- 136 M. Heuberger, M. Zach and N. D. Spencer, *Science*, 2001, **292**, 905–908.
- 137 J. W. Wang, A. G. Kalinichev and R. J. Kirkpatrick, *Geochim. Cosmochim. Acta*, 2004, **68**, 3351–3365.
- 138 R. Knochenmuss, *Eur. J. Mass Spectrom.*, 2009, **15**, 189–198.
- 139 G. H. Luo, Y. Chen, G. Siuzdak and A. Vertes, *J. Phys. Chem. B*, 2005, **109**, 24450–24456.
- 140 V. E. Frankevich, J. Zhang, S. D. Friess, M. Dashtiev and R. Zenobi, *Anal. Chem.*, 2003, **75**, 6063–6067.
- 141 R. Knochenmuss, G. McCombie and M. Faderl, *J. Phys. Chem. A*, 2006, **110**, 12728–12733.
- 142 V. Zorba, P. Tzanetakis, C. Fotakis, E. Spanakis, E. Stratakis, D. G. Papazoglou and I. Zergioti, *Appl. Phys. Lett.*, 2006, **88**, 081103.
- 143 Q. Liu and L. He, *J. Am. Soc. Mass Spectrom.*, 2008, **19**, 8–13.
- 144 B. N. Walker, G. Pasmanik and A. Vertes, *Laser Desorption Ionization from Laser Induced Silicon Microcolumns: Surface Morphology and Chemistry*, New Orleans, LA, USA, 2008.
- 145 Y. F. Chen, H. Y. Chen, A. Aleksandrov and T. M. Orlando, *J. Phys. Chem. C*, 2008, **112**, 6953–6960.
- 146 Z. X. Shen, J. J. Thomas, C. Averbuj, K. M. Broo, M. Engelhard, J. E. Crowell, M. G. Finn and G. Siuzdak, *Anal. Chem.*, 2001, **73**, 612–619.
- 147 T. R. Northen, O. Yanes, M. T. Northen, D. Marrinucci, W. Uritboonthai, J. Apon, S. L. Gollidge, A. Nordstrom and G. Siuzdak, *Nature*, 2007, **449**, 1033.
- 148 B. Gulbakan, D. Park, M. C. Kang, K. Kecici, C. R. Martin, D. H. Powell and W. H. Tan, *Anal. Chem.*, 2010, **82**, 7566–7575.
- 149 E. T. Castellana and D. H. Russell, *Nano Lett.*, 2007, **7**, 3023–3025.
- 150 C. Y. Lo, J. Y. Lin, W. Y. Chen, C. T. Chen and Y. C. Chen, *J. Am. Soc. Mass Spectrom.*, 2008, **19**, 1014–1020.
- 151 Y. Ke, S. K. Kailasa, H. Wu and Z. Chen, *Talanta*, 2010, **83**, 178–184.
- 152 E. Guenin, M. Lecouvey and J. Hardouin, *Rapid Commun. Mass Spectrom.*, 2009, **23**, 1395–1400.
- 153 C. W. Tsao, P. Kumar, J. K. Liu and L. Devoe, *Anal. Chem.*, 2008, **80**, 2973–2981.
- 154 R. Nayak and D. R. Knapp, *Anal. Chem.*, 2007, **79**, 4950–4956.
- 155 S. D. Sherrod, A. J. Diaz, W. K. Russell, P. S. Cremer and D. H. Russell, *Anal. Chem.*, 2008, **80**, 6796–6799.
- 156 Z. J. Zhu, P. S. Ghosh, O. R. Miranda, R. W. Vachet and V. M. Rotello, *J. Am. Chem. Soc.*, 2008, **130**, 14139–14143.
- 157 Z. J. Zhu, V. M. Rotello and R. W. Vachet, *Analyst*, 2009, **134**, 2183–2188.
- 158 N. H. Finkel, B. G. Prevo, O. D. Velev and L. He, *Anal. Chem.*, 2005, **77**, 1088–1095.
- 159 A. Amantonico, L. Flamigni, R. Glaus and R. Zenobi, *Metabolomics*, 2009, **5**, 346–353.
- 160 A. Kraj, J. Jarzebinska, A. Gorecka-Drzazga, J. Dziuban and J. Silberring, *Rapid Commun. Mass Spectrom.*, 2006, **20**, 1969–1972.
- 161 X. J. Wen, S. Dagan and V. H. Wysocki, *Anal. Chem.*, 2007, **79**, 434–444.
- 162 R. A. Kruse, S. S. Rubakhin, E. V. Romanova, P. W. Bohn and J. V. Sweedler, *J. Mass Spectrom.*, 2001, **36**, 1317–1322.
- 163 S. Taira, Y. Sugiura, S. Moritake, S. Shimma, Y. Ichianagi and M. Setou, *Anal. Chem.*, 2008, **80**, 4761–4766.
- 164 B. Yan, Z. J. Zhu, O. R. Miranda, A. Chompoosor, V. M. Rotello and R. W. Vachet, *Anal. Bioanal. Chem.*, 2010, **396**, 1025–1035.
- 165 G. J. Patti, H. K. Woo, O. Yanes, L. Shriver, D. Thomas, W. Uritboonthai, J. V. Apon, R. Steenwyk, M. Manchester and G. Siuzdak, *Anal. Chem.*, 2010, **82**, 121–128.
- 166 H. K. Woo, T. R. Northen, O. Yanes and G. Siuzdak, *Nat. Protoc.*, 2008, **3**, 1341–1349.
- 167 C. L. Su and W. L. Tseng, *Anal. Chem.*, 2007, **79**, 1626–1633.
- 168 Y. Gholipour, S. L. Giudicessi, H. Nonami and R. Erra-Balsells, *Anal. Chem.*, 2010, **82**, 5518–5526.
- 169 H. Kawasaki, T. Yao, T. Suganuma, K. Okumura, Y. Iwaki, T. Yonezawa, T. Kikuchi and R. Arakawa, *Chem.–Eur. J.*, 2010, **16**, 10832–10843.
- 170 M. Shariatgorji, N. Amini and L. L. Ilag, *J. Nanopart. Res.*, 2009, **11**, 1509–1512.
- 171 D. B. Wall, J. W. Finch and S. A. Cohen, *Rapid Commun. Mass Spectrom.*, 2004, **18**, 1403–1406.
- 172 J. C. Meng, G. Siuzdak and M. G. Finn, *Chem. Commun.*, 2004, 2108–2109.
- 173 N. Aminlashgari, M. Shariatgorji, L. L. Ilag and M. Hakkarainen, *Anal. Methods*, 2011, **3**, 192–197.
- 174 N. Amini, M. Shariatgorji and G. Thorsen, *J. Am. Soc. Mass Spectrom.*, 2009, **20**, 1207–1213.
- 175 T. Watanabe, K. Okumura, H. Kawasaki and R. Arakawa, *J. Mass Spectrom.*, 2009, **44**, 1443–1451.
- 176 R. D. Lowe, E. J. Szili, P. Kirkbride, H. Thissen, G. Siuzdak and N. H. Voelcker, *Anal. Chem.*, 2010, **82**, 4201–4208.
- 177 K. Pihlainen, K. Grigoras, S. Franssila, R. Ketola, T. Kotiaho and R. Kostiainen, *J. Mass Spectrom.*, 2005, **40**, 539–545.
- 178 F. Rowell, K. Hudson and J. Seviour, *Analyst*, 2009, **134**, 701–707.
- 179 Z. X. Shen, J. J. Thomas, G. Siuzdak and R. D. Blackledge, *J. Forensic Sci.*, 2004, **49**, 1028–1035.
- 180 J. J. Thomas, Z. X. Shen, R. Blackledge and G. Siuzdak, *Anal. Chim. Acta*, 2001, **442**, 183–190.
- 181 D. S. Peterson, Q. Z. Luo, E. F. Hilder, F. Svec and J. M. J. Frechet, *Rapid Commun. Mass Spectrom.*, 2004, **18**, 1504–1512.
- 182 A. Kraj, M. Swist, A. Strugala, A. Parczewski and J. Silberring, *Eur. J. Mass Spectrom.*, 2006, **12**, 253–259.
- 183 H. Kawasaki, N. Takahashi, H. Fujimori, K. Okumura, T. Watanabe, C. Matsumura, S. Takemine, T. Nakano and R. Arakawa, *Rapid Commun. Mass Spectrom.*, 2009, **23**, 3323–3332.
- 184 H. Kawasaki, Y. Shimomae, T. Watanabe and R. Arakawa, *Colloids Surf., A*, 2009, **347**, 220–224.
- 185 L. G. Hu, S. Y. Xu, C. S. Pan, C. G. Yuan, H. F. Zou and G. B. Jiang, *Environ. Sci. Technol.*, 2005, **39**, 8442–8447.
- 186 J. Gopal, J. L. Narayana and H. F. Wu, *Biosens. Bioelectron.*, 2011, **27**, 201–206.
- 187 R. M. Caprioli, T. B. Farmer and J. Gile, *Anal. Chem.*, 1997, **69**, 4751–4760.
- 188 V. Vidova, P. Novak, M. Strohalm, J. Pol, V. Havlicek and M. Volny, *Anal. Chem.*, 2010, **82**, 4994–4997.
- 189 J. Forster, I. Famili, P. Fu, B. O. Palsson and J. Nielsen, *Genome Res.*, 2003, **13**, 244–253.
- 190 J. El-Ali, P. K. Sorger and K. F. Jensen, *Nature*, 2006, **442**, 403–411.
- 191 K. Huikko, P. Ostman, C. Sauber, F. Mandel, K. Grigoras, S. Franssila, T. Kotiaho and R. Kostiainen, *Rapid Commun. Mass Spectrom.*, 2003, **17**, 1339–1343.
- 192 C. H. Teng, K. C. Ho, Y. S. Lin and Y. C. Chen, *Anal. Chem.*, 2004, **76**, 4337–4342.

-
- 193 C. Wu, C. H. Crouch, L. Zhao, J. E. Carey, R. Younkin, J. A. Levinson, E. Mazur, R. M. Farrell, P. Gothoskar and A. Karger, *Appl. Phys. Lett.*, 2001, **78**, 1850–1852.
- 194 W. Ekardt, W. D. Schone and R. Keyling, *Appl. Phys. A: Mater. Sci. Process.*, 2000, **71**, 529–535.
- 195 W. D. Schone and W. Ekardt, *Phys. Rev. B: Condens. Matter Mater. Phys.*, 2002, **65**, 113112.
- 196 J. Cao, Y. Gao, H. E. Elsayed-Ali, R. J. D. Miller and D. A. Mantell, *Phys. Rev. B: Condens. Matter Mater. Phys.*, 1998, **58**, 10948–10952.
- 197 Z. Takats, J. M. Wiseman, B. Gologan and R. G. Cooks, *Science*, 2004, **306**, 471–473.
- 198 R. G. Cooks, Z. Ouyang, Z. Takats and J. M. Wiseman, *Science*, 2006, **311**, 1566–1570.
- 199 J. B. Fenn, M. Mann, C. K. Meng, S. F. Wong and C. M. Whitehouse, *Science*, 1989, **246**, 64–71.
- 200 M. Mann, C. K. Meng and J. B. Fenn, *Anal. Chem.*, 1989, **61**, 1702–1708.
- 201 J. B. Fenn, M. Mann, C. K. Meng, S. F. Wong and C. M. Whitehouse, *Mass Spectrom. Rev.*, 1990, **9**, 37–70.
- 202 P. Nemes and A. Vertes, *Anal. Chem.*, 2007, **79**, 8098–8106.
- 203 P. Nemes, A. S. Woods and A. Vertes, *Anal. Chem.*, 2010, **82**, 982–988.
- 204 B. Shrestha, J. M. Patt and A. Vertes, *Anal. Chem.*, 2011, **83**, 2947–2955.
- 205 K. Tanaka, H. Waki, Y. Ido, S. Akita, Y. Yoshida and T. Yoshida, *Rapid Commun. Mass Spectrom.*, 1988, **2**, 151–153.
- 206 F. Hillenkamp, M. Karas, R. C. Beavis and B. T. Chait, *Anal. Chem.*, 1991, **63**, A1193–A1202.